Dileptons in heavy-ion collisions

Hendrik van Hees[1,2]

[1]Institute for Theoretical Physics, Goethe University Frankfurt, Max-von-Laue-Straße 1, Frankfurt am Main, D-60438, Germany.
[2]Helmholtz Research Academy Hessen for FAIR (HFHF), GSI Helmholtz Center, Campus Frankfurt, Max-von-Laue-Straße 12, Frankfurt am Main, D-60438, Germany.

Contributing authors: hees@itp.uni-frankfurt.de;

Abstract

In this review we give an overview about dileptons as probes for the properties of the strongly interacting hot and dense matter created in heavy-ion collisions at various beam energies. As penetrating probes they leave the fireball unaffected from final-state interactions and thus provide a space-time-evolution weighted average of the in-medium properties of hot and dense QCD matter.

1 Introduction

One of the prime motivations for heavy-ion-collision experiments at a broad range of collision energies is to gain insight into the properties of the hot and dense medium consisting of strongly interacting particles. At the highest beam energies, as investigated at the Large Hadron Collider (CERN) and the Relativistic Heavy Ion Collider (RHIC) a state of this matter can be investigated, which is close to the situation in the very early universe (a few microseconds after the big bang), consisting of a strongly coupled plasma of quarks and gluons (QGP) at vanishing net-baryon density ($\mu_{\mathrm{B}} = 0$), which rapidly expands and cools undergoing a transition from partonic to hadronic "relevant degrees of freedom". In contradistinction to the hadronic observables, which reflect the properties of the medium at chemical freezeout, where the inelastic collision processes become ineffective, (via the particle abundancies, which are well described by the statistical hadronization model) and at thermal freezeout, from when on the hadrons stream freely to the detectors, for electromagnetic probes, i.e., photons and dileptons ($\mathrm{e}^+\mathrm{e}^-$ or $\mu^+\mu^-$ pairs), the QCD medium is transparent, and they are thus

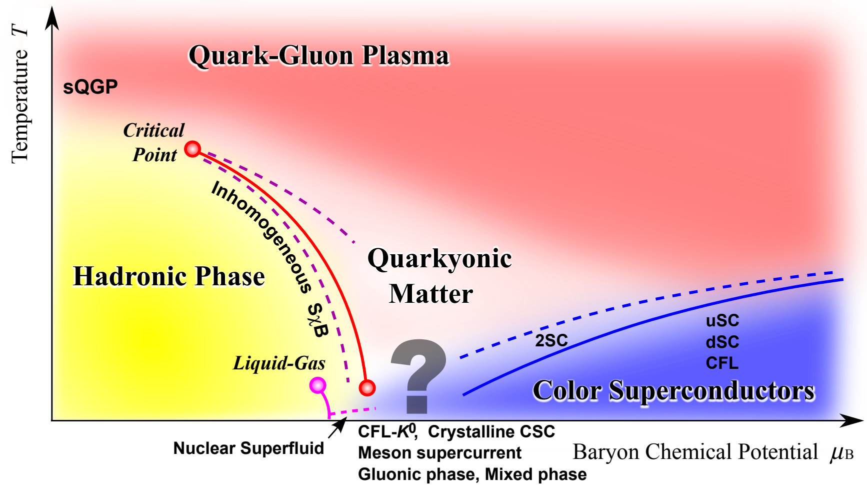

Fig. 1 Schematic QCD phase diagram with possible phase boundaries based on chiral symmetry. Figure taken from [1].

nearly unaffected by final-state interactions during the entire dynamical evolution of the hot and dense fireball. They are thus unique probes for the in-medium properties of quarks, gluons, and the hot and dense hadron-resonance gas. At lower beam energies, as investigated in the beam-energy scan (BES) program at RHIC and at GSI and in the future at FAIR, the fireball reaches lower temperatures and high net-baryon densities (finite μ_{B}), and with the BES one can hope to find clear indications for the onset of the formation of a QGP and the different phase transitions of the QCD medium expected from various theoretical models.

The phases of strongly interacting matter are thereby characterized by the approximate chiral symmetry of QCD in the light-quark sector with the quark condensate $\langle \bar{q} q \rangle \neq 0$ as an order parameter, while the confinement-deconfinement transition, where the effective degrees of freedom change between "hadronic" and "partonic" degrees of freedom. For this transition one uses Polyakov loops as indicators for the transition, although they are order parameters in the strict sense only in "quenched QCD", i.e., when dynamical quarks are neglected.

Theoretically the properties of the QCD medium at thermal equilibrium can be addressed from first principles by lattice-QCD (lQCD) calculations, which however is only applicable at $\mu_{\mathrm{B}} = 0$ or at low μ_{B}, due to the notorious "sign problem" at finite μ_{B}. In the region of the phase diagram close to the temperature axis lQCD shows that the confinement-deconfinement as well as the chiral transition are a crossover, both occuring at a temperature of about 155 MeV [2–4].

Although considerable progress has been made to overcome the problem to evaluate the QCD Equation of State (EoS) at $\mu_{\mathrm{B}} \neq 0$ with lQCD methods, here effective hadronic or quark-meson models based on chiral symmetry have to be used to explore possible scenarios for phase transitions from hadronic to partonic matter. Many of these models indicate that the phase transition at $T = 0$ is a first-order transition, i.e., in the T-μ_{B} plane one expects that at lower temperatures and large net-baryon densities a first-order transition line should occur, which ends at a critical point, where the transition becomes of 2$^{\mathrm{nd}}$ order. On the other hand some lQCD calculations indicate that such a critical point also might not exist [3].

Recently, many effective theories, based on the approximate chiral symmetry of QCD in the light-quark sector have been investigated at finite temperature and baryochemical potential. For a realistic description of the EoS also the gluonic degrees of freedom have to be considered to account for the confinement properties of QCD. For this purpose effective chiral models like the Nambu-Jona-Lasionio model [5–12] or quark-meson models (i.e., a linear σ model with quarks and mesons as elementary degrees of freedom) [13–18] have been generalized by the inclusion of Polyakov-loop degrees of freedom (so-called Polyakov-loop extended Nambu-Jona-Lasinio (PNJL) or quark-meson (PQM) models, respectively). These models can well reproduce the findings in lQCD calculations at vanishing or small baryochemical potential, and thus one may hope that they may also be successfully extrapolated to higher net-baryon densities. Here one needs the dependence of the deconfinement-transition temperature on quark-flavor number and density in the Polyakov-Loop potential, which are estimated with perturbative hard/dense-thermal-loop (HTL/DTL) techniques. E.g., within a PQM model [19] such techniques lead to the location of the critical point at a quite large baryochemical potential, $\mu_{\mathrm{B,crit}} \simeq 300$ MeV, and low temperature, $T_{\mathrm{crit}} \simeq 20$ MeV. At the same time the region, where chiral symmetry is restored but matter is still (effectively) confined ("quarkyonic state" predicted based on the large-N_{c} limit of QCD [20, 21]) becomes quite small.

For a realistic description of the QCD-phase diagram, calculations going beyond a pure mean-field model (Ginzburg-Landau approximation) are necessary, as the functional renormalization group [22–31].

The rest of this review is organized as follows: in Sect. 2 the general interpretation of dilepton-production data in heavy-ion collisions as a probe for the in-medium properties of the electromagnetic (e.m.) curren-current-correlation function is given and its relation with the (approximate) chiral symmetry of the light-quark sector of QCD is given.

In Sect. 3 we review models to describe the in-medium properties of quarks, gluons, and hadrons, the dynamical evolution of this medium as created in heavy-ion collisions.

In Sect. 4 we confront the before described models for in-medium dilepton production with data from heavy-ion collision experiments at a broad range of avialable beam energies.

2 General properties of dilepton emission from a QCD medium

For a realistic modelling of (thermal) dilepton production in heavy-ion collisions one needs both a model for the in-medium properties of strongly interacting constituents of the strongly interacting medium and a realistic model for the dynamical evolution of the rapidly expanding "fireballs" of this medium created in the collisions.

2.1 In-medium dilepton production rates

Following [32] and [33], we briefly discuss general ideas on the radiation of dileptons ($\mathrm{e}^+\mathrm{e}^-$ and $\mu^+\mu^-$ pairs) from a thermal source of strongly interacting particles. As indicated by the hadronic observables of heavy-ion collisions at higher beam energies, particularly p_T-spectra and anisotropic flow v_2, the hot and dense fireballs created in heavy-ion collisions behave with good accuracy like a collectively expanding fluid close to local thermal equilibrium, i.e., as a strongly coupled many-body system as far as the strong interaction is concerned. On the other hand the medium is transparent for leptons and photons that interact with the medium only via the electromagnetic and weak interactions. This implies that the radiation of electromagnetic probes can be expressed in terms of the equilibrium **electromagnetic current-current correlation function**, with the average taken in the fully interacting quantum field theory as far as the strong interaction is concerned and in leading order of the electromagnetic interaction, $\mathcal{O}(\alpha_\mathrm{em})$ for photons and $\mathcal{O}(\alpha_\mathrm{em}^2)$ for dileptons [34–36].

We derive the corresponding McLerran-Toimela formula for dileptons, assuming a (locally) equilibrated medium with a fluid cell at rest. The aim is to calculate the dilepton-production rate,

$$\frac{\mathrm{d}R_{\ell^+\ell^-}}{\mathrm{d}^4 k} = \frac{\mathrm{d}N_{\ell^+\ell^-}}{\mathrm{d}^4 x \mathrm{d}^4 k}, \tag{1}$$

i.e., the number of $\ell^+\ell^-$-pairs per time and volume and pair energy and momentum. To that end we work in an interaction picture with the "undisturbed Hamiltonian" fully including the strong interactions of quarks and gluons or hadrons and the "interaction Hamiltonian" given by the electromagnetic interaction

$$H_\mathrm{I} = e \int_{\mathbb{R}^3} \mathrm{d}^3\vec{x}\; J^\mu_\mathrm{em}(t,\vec{x}) A_\mu(t,\vec{x}). \tag{2}$$

On the fundamental level the electromagnetic current J^μ_em is given in terms of the charged leptons (charge -1) and the quarks by

$$\begin{split} J^\mu_\mathrm{em} = &-(\overline{\psi}_\mathrm{e}, \overline{\psi}_\mu, \overline{\psi}_\tau)\gamma^\mu \begin{pmatrix} \psi_\mathrm{e} \\ \psi_\mu \\ \psi_\tau \end{pmatrix} \\ &+ \frac{2}{3}(\overline{\psi}_u, \overline{\psi}_c, \overline{\psi}_t)\gamma^\mu \begin{pmatrix} \psi_\mathrm{u} \\ \psi_\mathrm{c} \\ \psi_t \end{pmatrix} - \frac{1}{3}(\overline{\psi}_d, \overline{\psi}_s, \overline{\psi}_b)\gamma^\mu \begin{pmatrix} \psi_\mathrm{d} \\ \psi_\mathrm{s} \\ \psi_b \end{pmatrix}. \end{split} \tag{3}$$

Working in leading order of the electromagnetic interaction, a schematic Feynman diagram for the transition-matrix element for the production of one $\ell^+\ell^-$ pair $|i\rangle \rightarrow |f'\rangle = |f, \ell^+\ell^-(k)\rangle$, where i and f are arbitrary partonic or hadronic initial and final states, is given by

$$S_{f'i} =$$

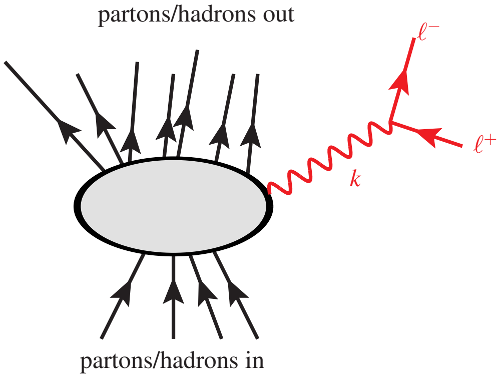

$$= e \left\langle f \left| \int \mathrm{d}^4 x J^{\mu}_{\mathrm{em}}(x) \right| i \right\rangle D_{\gamma}^{\mu\nu}(x,x')\overline{u_\ell}(x)\gamma_\nu v_\ell(x'). \tag{4}$$

Here u_ℓ and v_ℓ are the usual free Dirac spinors for the lepton and the antilepton in the final state, and $D_{\gamma}^{\mu\nu}$ is the photon propagator in an arbitrary gauge, e.g., in the Feynman gauge, where it reads in momentum representation

$$D_{\gamma}^{\mu\nu}(k) = -\frac{\eta^{\mu\nu}}{k^2 + \mathrm{i}0^+}. \tag{5}$$

In the momentum representation the matrix element reads

$$S_{f'i} = \mathrm{i}T_{f'i}(2\pi)^4 \delta^{(4)}(P_f + k - P_i) \tag{6}$$

and the dilepton-production rate according to "Fermi's trick" [37]

$$\frac{\mathrm{d}R}{\mathrm{d}^4 k} = (2\pi)^4 \left\langle \delta^{(4)}(P_f + k - P_i) |T_{f'i}|^2 \right\rangle \tag{7}$$

with the expectation value taken over all partonic/hadronic initial states with the (grand-canonical) equilibrium statistical operator, written in the local rest frame of the fluid cell,

$$\hat{\rho} = \frac{1}{Z} \exp\left[-\frac{1}{T}(\hat{H}_{\mathrm{QCD}} - \mu_{\mathrm{B}} \hat{Q}_{\mathrm{B}})\right], \quad Z = \mathrm{Tr} \exp\left[-\frac{1}{T}(\hat{H}_{\mathrm{QCD}} - \mu_{\mathrm{B}} \hat{Q}_{\mathrm{B}})\right]. \tag{8}$$

Here T is the fluid cell's temperature and μ_{B} the baryochemical potential to take into account the conservation of the net-baryon number under the strong and electromagnetic interactions. In (8) one also sums over all possible partonic/hadronic final states and the spin-degrees of freedom of the lepton and antilepton. Making use of the analytic properties of the retarded em. current-current-correlation function, the final result reads [36]

$$\frac{\mathrm{d}R_{\ell^+\ell^-}}{\mathrm{d}^4k} = \frac{\alpha_{\mathrm{em}}^2}{6\pi^3} \frac{k^2+2m_\ell^2}{(k^2)^2} \sqrt{1-\frac{4m_\ell^2}{k^2}} \eta_{\mu\nu} \rho_{\mathrm{em}}^{\mu\nu}(k) n_{\mathrm{B}}(k^0), \tag{9}$$

where the spectral function of the correlation function is given in terms of the electromagnetic spectral function

$$\rho_{\mathrm{em}}^{\mu\nu}(k) = -2\,\mathrm{Im}\,\Pi_{\mathrm{em,rest}}^{\mu\nu}(k) \tag{10}$$

with the retarded em. current-current correlation function (i.e., the in-medium photon polarization tensor), evaluated in the grand-canonical equilibrium state (8) and to any order concerning the strong interaction,

$$\mathrm{i}\Pi_{\mathrm{em,ret}}^{\mu\nu}(k) = \int_{\mathbb{R}^4} \mathrm{d}^4x \exp(\mathrm{i}k\cdot x) \left\langle \left[\hat{J}_{\mathrm{em}}^\mu(x), \hat{J}_{\mathrm{em}}^\nu(0)\right] \right\rangle_{T,\mu_{\mathrm{B}}} \Theta(x^0), \tag{11}$$

and

$$n_{\mathrm{B}}(k^0) = \frac{1}{\exp(k^0/T)-1} \tag{12}$$

denotes the Bose-Einstein distribution function. Thus, (9) implies that the measurement of the dilepton-production rate in heavy-ion collisions provides information about the em. current-current correlation function of strongly interacting matter in thermal equilibrium (10). According to the above derivation of (9) of course the measured dilepton spectra are only accessible as a space-time weighted average over the entire fireball evolution. This implies that modeling the dilepton production in heavy-ion collisions to interpret the corresponding data must include a comprehensive understanding of the relevant microscopic processes for dilepton production in the medium as well as a detailed description of the fireball evolution.

More recently also more differential aspects of the dilepton-production spectra have become of interest and in reach of experimental observation in terms of the polarization of thermal dileptons from heavy-ion collisions.

Angular dependencies in the dilepton production rate can be unravelled by resolving the angle, $\Omega_l = (\phi_l, \theta_l)$, of a single lepton relative to the virtual photon's momentum in the latter's rest frame [38–40]. It can be shown [41] that, in the local restframe of the fluid cell,

$$\frac{\mathrm{d}R_{\ell^+\ell^-}}{d^4k\,d\Omega_l} = \frac{\alpha^2}{32\pi^4 M^4} \sqrt{1-\frac{4m_\ell^2}{M^2}} \rho_{\mathrm{em}}^{\mu\nu} L_{\mu\nu} n_{\mathrm{B}}(k_0;T), \tag{13}$$

with the lepton tensor

$$L^{\mu\nu} = 2(q^2 g^{\mu\nu} - q^\mu q^\nu + \Delta l^\mu \Delta l^\nu)\ , \tag{14}$$

where $\Delta l^\mu = l^{+\mu} - l^{-\mu}$, and $l^\pm$ are the lepton four-momenta. More explicitly, the angular distribution takes the form

$$\begin{aligned}\frac{dN_{ll}}{d^4x\, d^4q\, d\Omega_l} \propto \Big(1 &+ \lambda_\theta \cos^2\theta_l \\ &+ \lambda_\phi \sin^2\theta_l \cos 2\phi_l + \lambda_{\theta\phi} \sin 2\theta_l \cos\phi_l \\ &+ \lambda_\phi^\perp \sin^2\theta_l \sin 2\phi_l + \lambda_{\theta\phi}^\perp \sin 2\theta_l \sin\phi_l\Big),\end{aligned} \tag{15}$$

where the λ's are the anisotropy coefficients.

Even in an isotropic thermal medium, nontrivial anisotropies in the angular distribution of the produced leptons occur, e.g., for basic hadronic and partonic sources ($\pi\pi$ vs. $q\bar{q}$ annihilation, respectively) at a few percent level [40]. In addition, the anisotropy of lepton pairs in the M = 1-1.5 GeV region might be able to distinguish whether the so-called "chiral mixing" between ρ and a_1 channels via πa_1 annihilation or $q\bar{q}$ annihilation is the dominant source.

One should note that various "frames of reference" of the anisotropy coefficients are used in high-energy particle physics [42].

For theoretical investigations for the case of a static thermal medium the natural reference frame is the (local) rest frame of the fluid cell, defined by its four-velocity, $u' = \gamma(1, \vec{\beta}) = (1, 0, 0, 0)$. In this frame the rotational symmetry concerning the dilepton-emission rate is only broken by the virtual photon's momentum direction. Taking the polarization axis as the z'-axis in this frame of reference, defining the helicity frame HX$'$, the only non-vanishing anisotropy is given by

$$\lambda_\theta^{\mathrm{HX}'}(M, |\vec{q}|) = \frac{\varrho_{\mathrm{T}} - \varrho_{\mathrm{L}}}{\varrho_{\mathrm{T}} + \varrho_{\mathrm{L}}} \ , \tag{16}$$

where the photon-polarization tensor is given by the spatially transverse and longitudinal components,

$$\rho_{\mathrm{em}}^{\mu\nu} = \rho_{\mathrm{T}} \Theta_{\mathrm{T}}^{\mu\nu} + \rho_{\mathrm{L}} \Theta_{\mathrm{L}}^{\mu\nu} \tag{17}$$

with the decomposition of the four-transverse tensor wrt. the four-momentum dilepton (virtual photons) of invariant mass M,

$$\Theta^{\mu\nu}(q) = \eta^{\mu\nu} - \frac{q^\mu q^\nu}{M^2}, \tag{18}$$

$$(\Theta_{\mathrm{T}}^{\mu\nu}(q)) = \begin{pmatrix} 0 & \vec{0}^{\mathrm{T}} \\ \vec{0} & \left(-\delta^{jk} + q^j q^k / \vec{q}^2\right) \end{pmatrix}, \tag{19}$$

$$\Theta_{\mathrm{L}}^{\mu\nu}(q) = \Theta^{\mu\nu}(q) - \Theta_{\mathrm{T}}^{\mu\nu}. \tag{20}$$

For measurements in heavy-ion experiments, of course one must define a polarization observable with respect to an experimentally well-defined reference frame.

To define the socalled helicity frame (HX), we start from the virtual photon with four-momentum $k^\mu = (k_0, 0, 0, k)$ in the center-momentum system (CMS) of the collision, defining the z-axis along its three-momentum, $\vec{k}$. In the helicity frame (HX) this defines the polarization axis while the pertinent y-axis is defined by the normal vector in the plane spanned by the beam momenta, and thus defines the (xyz) system. On the other hand, the z' axis is defined in the thermal rest frame, which is moving with the medium's flow velocity u^μ in the CMS.

The photon four-momentum in this system, q^μ, is obtained from the Lorentz boost of k^μ using u^μ, and determines the only non-vanishing coefficient in this system, $\lambda_\theta^{\mathrm{HX}'}$. With the above definitions, one can then transform the angular distribution into the HX system by a succession of three Euler rotations:

(i) around the z'-axis by an angle ψ to bring the y-axis perpendicular to the z-axis;
(ii) around the thus obtained y'' axis by an angle ζ to align the z'-axis with the z-axis; and
(iii) around the z-axis by an angle ω to align the x'- and y'-axes along the x- and y-axes, respectively. In this way, all five coefficients in Eq. (15) can be determined from $\lambda_\theta^{\mathrm{HX}'}$ and the three rotation angles described above.

In a similar way also the description of the measurements in the Collins-Soper (CS) frame of reference have to be descriped. In the CS frame the quantization axis is defined as the bisector between the projectile and target momentum in the restframe of the dilepton (virtual photon) [42].

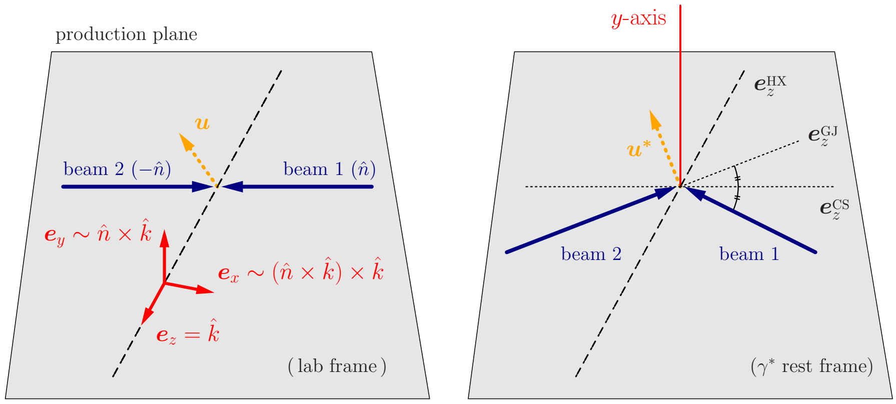

Fig. 2 The definition of the various reference frames for defining polarization observables. The choice of the spin-quantization axis $\vec{e}_z$ is defines the various frames. Helicity frame (HX): $vece_z$ is the direction of the virtual-photon (γ^*) momentum in the lab frame, Collins-Soper frame (CS): $\vec{e}_z$ is in the direction of the bisector of angle between the direction of one beam and the opposite of the direction of the other, as measured in the γ^* rest frame , and Gottfried-Jackson frame (GJ): $\vec{e}_z$ is in the direction of one of the beams in the γ^* fest frame (for details, see [42]). Figure taken from [43].

2.2 Dileptons and chiral symmetry

In this Section we discuss the relation of the electromagnetic current-correlation function in a strongly interacting medium to the approximate chiral $\mathrm{SU}(2)_{\mathrm{L}} \times \mathrm{SU}(2)_{\mathrm{R}} \times \mathrm{U}(1)_{\mathrm{V}}$ symmetry of QCD.

On the fundamental level of the Standard Model the key is the decomposition of the light (u- and d-) quarks' electromagnetic current

$$J_{\text{em,ud}} = \frac{2}{3}\overline{\psi_{\text{u}}}\gamma^{\mu}\psi_{\text{u}} - \frac{1}{3}\overline{\psi_{\text{d}}}\gamma^{\mu}\psi_{\text{d}}, \tag{21}$$

cf. (3), in an isovector and an isoscalar component. To that end we just have to remember that the electrically neutral component of the isovector current is given by

$$J_{\text{V}}^{3\mu} = \overline{\psi}_{\text{ud}} t^3 \gamma^{\mu}\psi_{\text{ud}} = \frac{1}{2}\left(\overline{\psi}_{\text{u}}\gamma^{\mu}\psi_{\text{u}} - \overline{\psi}_{d}\gamma^{\mu}\psi_{\text{d}}\right), \tag{22}$$

which carries the quantum numbers of the neutral $\rho(770)$ meson. The isoscalar current reads

$$j_{\text{V}}^{\mu} = \overline{\psi}_{\text{u}}\gamma^{\mu}\psi_{\text{u}} + \overline{\psi}_{d}\gamma^{\mu}\psi_{\text{d}}, \tag{23}$$

which carries the quantum numbers of the $\omega(770)$ meson. Now, as is immediately clear from (21-23) the electromagnetic current (21) can be written as

$$J_{\text{em,ud}}^{\mu} = J_{\text{V}}^{3\mu} + \frac{1}{6} j_{\text{V}}^{\mu}. \tag{24}$$

To extend this pattern to also include the strange quark[1] we only have to add $J_{\text{em,s}}^{\mu} = -1/3\overline{\psi_{\text{s}}}\gamma^{\mu}\psi_{\text{s}}$ to (21). Then we can write the electromagnetic current of the three light quarks in the form

$$\begin{aligned} J_{\text{em,uds}} = \frac{1}{\sqrt{2}}\Bigg[&\frac{1}{\sqrt{2}}\left(\overline{\psi}_{\text{u}}\gamma^{\mu}\psi_{\text{u}} - \overline{\psi}_{d}\gamma^{\mu}\psi_{\text{d}}\right) \\ &+ \frac{1}{3\sqrt{2}}\left(\overline{\psi}_{\text{u}}\gamma^{\mu}\psi_{\text{u}} + \overline{\psi}_{d}\gamma^{\mu}\psi_{\text{d}}\right) - \frac{\sqrt{2}}{3}\overline{\psi}_{\text{s}}\gamma^{\mu}\psi_{\text{s}}\Bigg]. \end{aligned} \tag{25}$$

It is suggestive to associate the three terms in the bracket with the corresponding light vector mesons ρ, ω, and ϕ. The relative weights in the electromagnetic current correlation function is thus 9:1:2. Empirically the partial decay widths of the light vector mesons to dielectrons are $\Gamma_{\rho\to\text{e}^+\text{e}^-}/\Gamma_{\omega\to\text{e}^+\text{e}^-} \simeq 10.5$ and $\Gamma_{\phi\to\text{e}^+\text{e}^-}/\Gamma_{\omega\to\text{e}^+\text{e}^-} \simeq 1.9$ [44], which is not too far from the naive parton argument based on (25).

In hadronic models the assumption that the hadronic electromagnetic current is proportional to the neutral vector-meson fields, the so-called **vector-meson dominance model (VMD)** [45–47] leads to a quite successful description of hadronic electromagnetic transition form factors, particularly the electromagnetic form factor of the pion.

[1]Since also the strange-quark mass is small compared to the typical hadronic scale of 1 GeVone can extend the approximate chiral $\text{SU}(2)_{\text{L}} \times \text{SU}(2)_{\text{R}} \times \text{U}(1)_{\text{V}}$ symmetry of the ud-quark sector of QCD to the uds-quark sector with the symmetry group $\text{SU}(3)_{\text{L}} \times \text{SU}(3)_{\text{R}} \times \text{U}(1)_{\text{V}}$. The symmetry is spontaneously broken to $\text{SU}(3)_{\text{V}} \times \text{U}(1)_{\text{V}}$ and of course also explicitly broken by the quark masses and the electroweak interactions. The pseudo-Goldstone bosons are grouped into the pseudoscalar SU(3) octet, consisting of the 3 pions, 4 kaons, and one η^0.

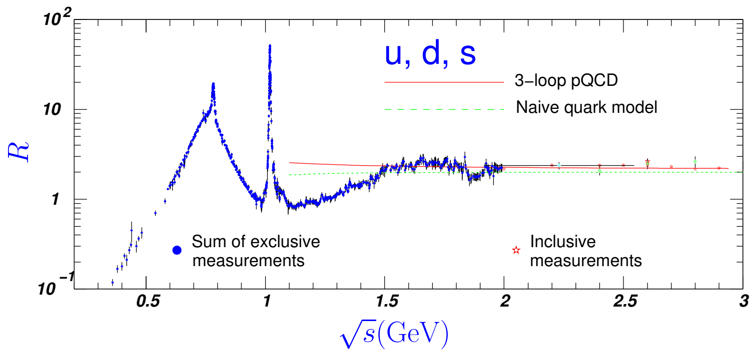

Fig. 3 The ratio $\sigma_{\mathrm{e}^+ + \mathrm{e}^- \to \mathrm{hadrons}}/\sigma_{\mathrm{e}^+ + \mathrm{e}^- \to \mu^+ + \mu^-}$ in the low- and intermediate-mass region. Figure taken from [48].

Very accurate measurements of the hadronic em. current-current-correlation function are provided by the inclusive hadron production in the reaction $\mathrm{e}^+ + \mathrm{e}^- \to$ hadrons, which is usually depicted in terms of the ratio

$$R = \frac{\sigma_{\mathrm{e}^+ + \mathrm{e}^- \to \mathrm{hadrons}}}{\sigma_{\mathrm{e}^+ + \mathrm{e}^- \to \mu^+ + \mu^-}}, \tag{26}$$

as shown in Fig. 3 as a function of the invariant mass of the electron-positron pair $M = \sqrt{s}$. The low-mass region $2m_{\mathrm{e}} \leq M \lesssim m_\phi$ is dominated by the three light vector mesons, ρ, ω, and ϕ, followed in the intermediate-mass region $m_\phi \lesssim M \lesssim M_{J/\psi}$ by a broader vector-meson resonance ρ' and a continuum that is well-described in the naive parton model, where the ratio is given by

$$R_{\text{parton model}} = N_c \sum_{f \in \{\mathrm{u,d,s}\}} q_f^2 = 3\left(\frac{4}{9} + 2 \cdot \frac{1}{9}\right) = 2. \tag{27}$$

From the electroweak sector of the Standard Model it is known that the vector and axial-vector strong-isovector current-correlation functions are directly related to the charged electroweak current, which is of the clean "$V - A$ structure" (see, e.g., [49]). Taking into account parity conservation of the strong interaction it is clear that the semileptonic decay $\tau \to \nu_\tau +$pions of τ-leptons together with the known weak coupling constant (or equivalently the Fermi constant in the effective four-fermion model) and the relevant CKM-matrix element $|V_{ud}|$ allows for an accurate quantitative separation of the current-correlation functions into the isovector- and axial-vector channel by exclusive measurements of the partial τ-lepton decay widths into an even or odd number of pions respectively. As shown in Fig. 4 these data can be interpreted as an accurate demonstration of the spontaneous breaking of the (approximate) chiral symmetry of QCD in the light-quark sector.

One of the fundamental questions addressed with the accurate measurement of dileptons in heavy-ion collisions is to learn about how this chiral symmetry of QCD is realized at low energies, i.e., in which way the dynamical generation of hadron

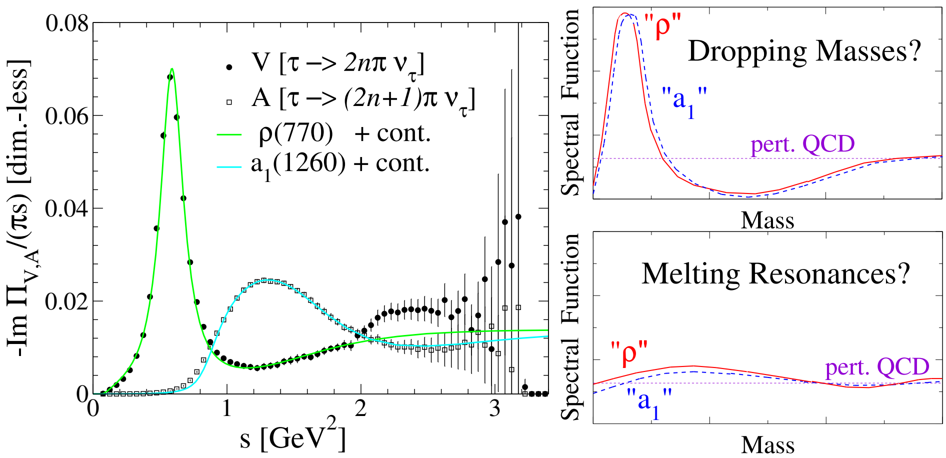

Fig. 4 Left panel: The isovector-vector and -axial-vector current correlation functions as a function of the total center-momentum energy of the pions ($s = E_{\text{cm}}^2$) as extracted from τ-lepton decay to an even and odd number of pions [50] together with model fits with vacuum ρ- and a_1-meson spectral functions and a perturbative continuum [51]. Right panel: Possible scenarios for the effect of chiral-symmetry restoration to the vector-axial-vector spectral functions in the hot and dense medium. Figure taken from [33].

masses by the strong interaction comes about, at least for the ρ meson, which dominates the electromagnetic current-current correlation function in the low-mass region, as explained above. As the detailed analysis of effective hadronic models shows, chiral symmetry of the light vector bosons can be realized in (at least) two possible ways. E.g. in terms of "hidden-local-symmetry models", which describe the massive vector (ρ) and in its generalized version also the axial-vector (a_1) meson with a "Higgsed" additional local chiral gauge symmetry (usually realized in a non-linear way) [52–54]. It can be realized either by introducing only the ρ-meson as a gauge field, corresponding to the unbroken part $\mathrm{SU(2)_V}$ of the $\mathrm{SU(2)_L \times SU(2)_R}$ or both a ρ and an a_1 meson. In this kind of models chiral symmetry can be realized in the so-called vector manifestation, where in the model introducing only the ρ-meson the longitudinal component of the ρ meson becomes the chiral partner of the pions, which leads to a dropping mass towards the chiral phase transition. On the other hand, even in the same class of models, also the realization of chiral symmetry is possible, where the chiral partners are ρ and a_1, and the mass spectra of these two mesons become degenerate by a large broadening of their spectral functions in the medium [55, 56].

3 Models for electromagnetic probes in heavy-ion collisions

To address the production of dileptons in heavy-ion collisions, the medium modification of the em. current-current correlator entering the production rate as discussed in Sect. 2.1, cf. (9) has to be evaluated. At higher collision energies the produced matter becomes hot and dense enough to enter the deconfined phase of a quark-gluon

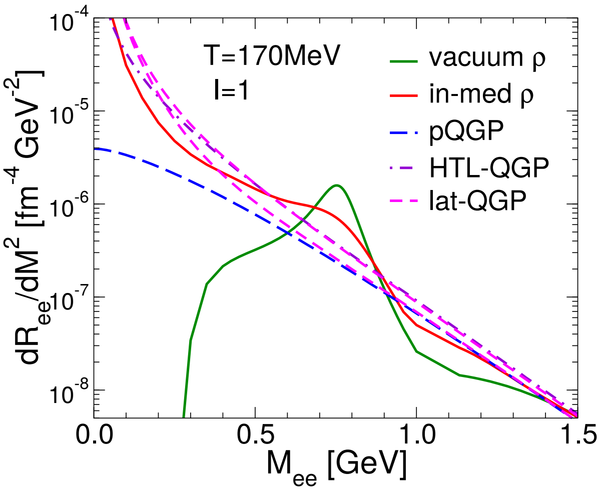

Fig. 5 Dilepton-emission rate as a function of invariant mass at $T = 170$ MeV from $q\overline{q} \rightarrow \ell^+\ell^-$ annihilation in leading order perturbation theory (blue line), a leading-order hard-thermal loop calculation (violet line), and a lattice-QCD (red line) in comparison to the calculation from hadronic effective theory with and without medium effects. Fig. taken from [57].

plasma and then evolves as an expanding and cooling fireball undergoing the transition to a hot and dense hadron-resonance gas that finally decouples to freely streaming hadrons observed in the detectors.

As a comparison of the found particle abundances and spectra with relativistic hydrodynamic simulations shows, that the hot and dense fireball in this evolution is well described by a medium close to local thermal equilibrium. This allows the use of the equilibrium in-medium electromagnetic current-current correlation function (9) to describe the dilepton-production rate in heavy-ion collisions. Since the electromagnetic probes are emitted during the entire evolution of the medium, both a detailed description of this collective dynamics of the medium as well as the production rates are necessary over a wide range of temperatures and baryochemical potentials. In the following we first briefly describe the quantum-field theoretical models for the in-medium production rates and then the bulk-evolution models.

3.1 Electromagnetic radiation from the QGP

At leading order (LO) in α_{em}, the basic process for dilepton production in the partonic phase is q-$\overline{q}$ annihilation, $q+\overline{q} \rightarrow \ell^- + \ell^+$. In terms of the current-current correlation function, which in quantum-field theoretical view is just given by the photon polarization function, this refers to the one-loop diagram,

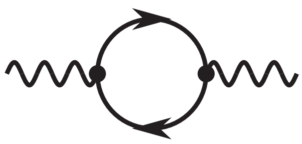

.

Its evaluation leads to the dilepton production rate from the QGP at temperature T and quark-chemical potential $\mu_\mathrm{q} = \mu_\mathrm{B}/3$ [58].

$$\begin{aligned}\operatorname{Im}\Pi_{\mathrm{em}}^{(\mathrm{QGP})}(k) &= -\sum_f q_f^2 \frac{N_c}{12\pi} \frac{Tk^2}{\left|\vec{k}\right|} \ln\left(\frac{\{x_- + \exp[-(k^0+\mu)/T]\}[x_+ + \exp(-\mu/T)]}{\{x_+ + \exp[-(k^0+\mu)/T]\}[x_- + \exp(-\mu/T)]}\right) \\ &= \frac{C_\mathrm{em} N_\mathrm{c}}{12\pi} M^2 \hat{f}_2(k_0, k; T)\end{aligned} \tag{28}$$

with

$$x_\pm = \exp\left(-\frac{E_\pm}{T}\right), \quad E_\pm = \frac{1}{2}(k^0 \pm \left|\vec{k}\right|). \tag{29}$$

However, at lower invariant dilepton masses the rate is tremendously enhanced by taking into account the leading-order α_s corrections employing the hard-thermal-loop (HTL) resummation techniques to dress the quark propagators [59]: Although both, quarks and gluons, acquire a thermal mass $\sim gT$ bremsstrahlung contributions within the HTL resummation leads to an enhancement of the dilepton-production rates down to the two-lepton threshold (cf. Fig. 5).

The dilepton-production rates have also been calculated in thermal lattice QCD [60–62]. Here the Euclidean-time vector-current correlation function,

$$\Pi_B(\tau, q; T) = \int_0^\infty \frac{\mathrm{d}q_0}{2\pi} \rho_V(q_0, q, T) \frac{\cosh[q_0(\tau - 1/2T)]}{\sinh(q_0/2T)}, \tag{30}$$

is evaluated in quenched QCD for $T = 1.45 T_\mathrm{c}$ at $q = 0$. The spectral function is obtained from these numerical results by fitting the parameters Γ and κ in the ansatz

$$\rho_V(q_0) = S_\mathrm{BW} \frac{q_0 \Gamma/2}{q_0^2 + \Gamma^2/4} + \frac{C_\mathrm{em} N_\mathrm{c}}{2\pi}(1+\kappa) q_0^2 \tanh(q_0/2T) \tag{31}$$

for the spectral function to the numerical results for (30).

To use the corresponding dilepton rates in calculations to describe heavy-ion collisions an extrapolation to finite three-momentum is needed. In [57] such an extrapolation is provided by using the transverse part of the electromagnetic spectral function from the leading-order pQCD photon rate for the three-momentum dependence of the spectral function (31), replacing the Breit-Wigner piece. This finally leads to the parameterization

$$\begin{aligned}\operatorname{Im}\Pi_\mathrm{T} &= -\frac{C_\mathrm{em}}{12\pi} M^2 \left[\hat{f}_2\left(k_0, \left|\vec{k}\right|; T\right) + 2\pi\alpha_\mathrm{s} \frac{T^2}{M^2} K F(M^2) \ln\left(1 + \frac{2.912 k_0}{4\pi\alpha_\mathrm{s} T}\right)\right] \\ &= \frac{C_\mathrm{em} N_\mathrm{c}}{12\pi} M^2 \left[\hat{f}_2\left(k_0, \left|\vec{k}\right|; T\right) + Q_\mathrm{lat}^{(\mathrm{T})}\left(k_0, \left|\vec{k}\right|\right)\right].\end{aligned} \tag{32}$$

Here $K = 2$ is introduced to account for the enhancement of the photon rate over the LO rate and to better reproduce the low-energy limit of the lattice-QCD spectral function. To accommodate the behavior at higher energies, an additional form factor $F(M^2) = \Lambda^2/(\Lambda^2+M^2)$ with $\Lambda = 2T$ has been used. In Fig. 5 the upper (lower) dashed line corresponds to this parameterization with (without) this form factor. Finally one has to also reconstruct the longitudinal part of the current-correlation function. This is achieved by using the standard construction of gauge-invariant s-wave ρ-baryon interactions, $\Pi_L = (M^2/q_0^2)\Pi_T$ [63].

3.2 Electromagnetic radiation from a hot/dense hadron gas

At lower temperatures and densities the low-mass dilepton spectrum is governed by the in-medium spectral functions of the light vector mesons, ρ, ω, and ϕ in the sense of the vector-meson dominance model. For the description of this contribution to the dilepton rate in heavy-ion collisions we use the "Rapp-Wambach Model" based on [64–68] as summarized in [69]. The evaluation of the spectral properties of the vector mesons in a dense and hot hadronic medium consists in the determination of their self-energies in thermal and chemical equilibrium. Here we concentrate on the ρ meson. Microscopically the corresponding in-medium contributions consist (i) the modification of the pion loop in the $\rho\pi\pi$ loop and (ii) via direct couplings of the ρ meson to both mesons and baryons. As will become clear, particularly the baryon contributions play a crucial role in describing the dilepton spectra in heavy-ion collisions at all energies. Although at the highest available collision energies at RHIC and LHC the net-baryon density is low ($\mu_{\mathrm{B}} \simeq 0$), the total baryon density $n_{\mathrm{B}} + n_{\overline{\mathrm{B}}}$ is high, and thus leads to significant modifications of the ρ-meson spectral function, contributing particularly in the low-mass tail of the dilepton invariant-mass spectrum.

The $\rho\pi\pi$ interaction is based on the interaction Lagrangian [64, 65]

$$\mathscr{L}_{\rho\pi\pi} = g_{\rho\pi\pi}(\vec{\pi} \times \partial^\mu \vec{\pi}) \cdot \vec{\rho}_\mu \tag{33}$$

with $\vec{\pi}$ and $\vec{\rho}_\mu$ the isovector pion and isovector ρ-meson fields, respectively. To account for medium modifications of the pion, the pion self-energy Σ_π is evaluated employing particle-hole excitations [70, 71], where the pions interact with nucleons and Δ resonances through particle-hole excitations of the type NN^{-1}, ΔN^{-1}, $N\Delta^{-1}$, and $\Delta\Delta^{-1}$. In order to guarantee the transversality of the ρ self-energy the corresponding vertex corrections to restore the pertinent Ward-Takahashi identities have to be taken into account [66]. The needed ρN and $\rho\pi N$ couplings are obtained from the pionic Lagrangian by minimal coupling to the πN couplings,

$$\begin{aligned} \mathscr{L}_{\rho N} &= -\frac{g}{2}\overline{\psi}\not{\rho}\tau_3\psi, \\ \mathscr{L}_{\rho\pi N} &= \mathrm{i}g\frac{f_N}{m_\pi}\overline{\psi}\gamma^5\not{\rho}\vec{\tau}\psi \cdot T_3\vec{\pi}, \end{aligned} \tag{34}$$

and the $\pi\Delta$ couplings,

$$\begin{aligned}\mathscr{L}_{\rho\Delta} &= g\overline{\psi}_\mu \not{\rho} T_3^{(3/2)}\psi^\mu - \frac{g}{3}\overline{\psi}_\mu(\gamma^\mu\rho_\nu + \gamma_\nu\rho^\mu)T_3^{(3/2)}\psi^\nu \\ &\quad + \frac{g}{3}\overline{\psi}_\mu\gamma^\mu\not{\rho} T_3^{(3/2)}\gamma_\nu\psi^\nu, \\ \mathscr{L}_{\rho\pi N\Delta} &= -\mathrm{i}g\frac{f_\Delta}{m_\pi}\overline{\psi}T^\dagger\psi_\mu\rho^\mu\cdot T_3\vec{\phi} + \text{h.c.}\end{aligned} \tag{35}$$

One way to fix the various parameters in the model is to aim at a description of data on photon absorption on nucleons and nuclei. For that purpose the direct coupling of the ρ meson to various baryon resonances has to be addressed [67]. The corresponding interaction Lagrangians are given by p-wave couplings of positive parity states and s-wave couplings of negative-parity states to the ρN system, which read in the here employed non-relativistic limit

$$\begin{aligned}\mathscr{L}_{\rho BN}^{(\text{p-wave})} &= \frac{f_{\rho BN}}{m_\rho}\Psi_B^\dagger(\vec{s}\times\vec{q})\cdot\vec{\rho}_a t_a \Psi_N + \text{h.c.}, \\ \mathscr{L}_{\rho BN}^{(\text{s-wave})} &= \frac{f_{\rho BN}}{m_\rho}\Psi_B^\dagger(q_0\vec{s}\cdot\vec{\rho}_a - \rho_a^0\vec{s}\cdot\vec{q})t_a\Psi_N + \text{h.c.}\end{aligned} \tag{36}$$

Here, $\vec{s}$ denote spin (transition) operators for $J = 1/2$ and $J = 3/2$ and t the isospin (transition) operators for $I = 1/2$ and $I = 3/2$, depending on the quantum numbers of the baryons, $B = \mathrm{N}(939)$, $\Delta(1232)$, N(1720) (positive parity) as well as $B = \mathrm{N}(1520)$, $\Delta(1620)$, $\Delta(1700)$ (negative parity). For the spin-5/2 $\Delta(1905)$ a tensor coupling of the type $(R_{ij}q_i\rho_{j,a}T_a)$ is employed.

The in-medium self-energies from the resulting baryon nucleon-hole loop diagrams are of the form

$$\Sigma_{\rho\alpha}^{(0),T}(q_0,q) = -\left(\frac{f_{\rho\alpha}F_{\rho\alpha}(q)}{m_\rho}\right)\mathrm{SI}(\rho\alpha)Q^2\phi_{\rho\alpha}(q_0,q), \tag{37}$$

where $Q^2 = q^2, q_0^2$ for p- and s-wave couplings, respectively. Also a monopole form factor $F_{\rho\alpha}(q) = \Lambda_\rho^2/(\Lambda_\rho^2+q^2)$ has been introduced, and $\mathrm{SI}(\rho\alpha)$ denotes the spin-isospin factor; $\phi_{\rho\alpha}(q_0,q)$ is the Lindhard function corresponding to the one-loop self-energy diagram. The photoabsorption cross section within the strict vector-meson dominance model reads

$$\frac{\sigma_{\gamma A}^{\text{abs}}}{A} = -\frac{4\pi\alpha_{\text{em}}}{q_0}\frac{(m_\rho^{(0)})^4}{g^2}\frac{1}{\rho_N}\,\mathrm{Im}\,D_\rho^T(q_0,\vec{q};\rho_N). \tag{38}$$

On the other hand it is known that this strict realization of the vector-meson dominance ansatz tends to overestimate the $B\to N\gamma$ branching fractions with the hadronic couplings determined from the corresponding $B\to\rho N$ decay widths. This can, however, be corrected by using the extended realization of VMD in [47], which allows to adjust the BNγ coupling at the photon point independently [75]. As shown in Fig. 6, making use of this freedom a satisfactory fit to the data on photoabsorption on protons as well as nuclei can be achieved, resulting in the values of the various coupling constants given in Table 1.

B	$l_{\rho N}$	SI(ρBN^{-1})	$\Gamma^0_{\rho N}$ (MeV)	$\left(\frac{f^2_{\rho BN}}{4\pi}\right)_{\text{est}}$	$\left(\frac{f^2_{\rho BN}}{4\pi}\right)_{\text{fit}}$	Γ^{med} [MeV]
N(939)	p	4	–	4.68	5.8	0
$\Delta(1232)$	p	16/9	–	18.72	23.2	15
$N(1520)$	s	8/3	24	6.95	5.5	250
$\Delta(1620)$	s	8/3	22.5	1.01	0.7	50
$\Delta(1700)$	s	16/9	45	1.2	1.2	50
$N(1720)$	p	8/3	105	8.99	9.2	50
$\Delta(1905)$	p	4/5	210	17.6	18.5	50

Table 1 Properties of the ρBN vertices as derived from the interaction Lagrangians (36); columns from left to right: baryon resonance, relative angular momentum in the ρN decay, spin-isospin factor, partial decay width into ρN as extracted from [72, 73], coupling constant as estimated from $\Gamma^0_{\rho N}$ (for N(939) and $\Delta(1232)$ we have indicated the values from the BONN potential [74] which uses somewhat harder form factors), coupling constant as in the fit to photoabsorption data, in-medium correction to the total decay width (cf. Fig. 6). Table taken from [67].

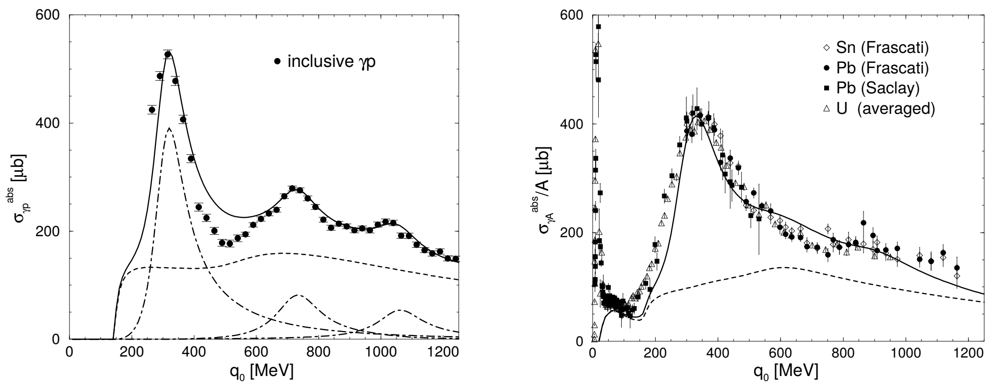

Fig. 6 Left panel: Total photoabsorption cross section on the proton. The solid line represents the full result of the fit of the model; the dashed lines show the $\pi\pi$ non-resonant background and the three dominant ρN resonances $\Delta(1232)$, N(1520), and N(1720). The data are from [76]. Right panel: Total photoabsorption cross section on various nuclei. The solid line represents the full result of the in-medium model calculation and the short-dashed line the $\pi\pi$ background, both calculated at a nuclear density $\overline{\varrho}_{\text{N}} = 0.8\varrho_0$. The long-dashed line corresponds to a linear-density approximation, reflecting the line shape of the left figure. The data are taken from [77–82]. The figures are taken from [67].

Finally the in-medium modifications of the ρ meson due to direct interactions with various mesons has to be taken into account [68]. At temperatures relevant for the hadron-gas phase of the medium created in heavy-ion collisions the most abundant hadrons are the pseudoscalar pseudo-Goldstone mesons $P = \pi$, K. So the heavier mesons can be treated as "ρP states", i.e., vector (V) and axial-vector mesons (A). The corresponding interaction Lagrangians, obeying chiral symmetry and (via the VMD conjecture) electromagnetic gauge invariance read

$$\begin{aligned} \mathscr{L}_{\rho PA} &= G_{\rho PA} A_\mu (\eta^{\mu\nu} q_\alpha p^\alpha - q^{mu} p^\nu) \rho_\nu P, \\ \mathscr{L}_{\rho PV} &= G_{\rho PV} \epsilon_{\mu\nu\rho\sigma} k^\mu V^\nu q^\rho \rho^\sigma P, \end{aligned} \tag{39}$$

R	$I^G J^P$	$\Gamma_{\rm tot}$ (MeV)	ρh Decay	$\Gamma^0_{\rho h}$ (MeV)	$\Gamma^0_{\gamma h}$ (MeV)
$\omega(782)$	0^-1^-	8.43	$\rho\pi$	~ 5	0.72
$h_1(1170)$	0^-1^+	~ 360	$\rho\pi$	seen	?
$a_1(1260)$	1^-1^+	~ 400	$\rho\pi$	dominant	0.64
$K_1(1270)$	$\frac{1}{2}1^+$	~ 90	ρK	~ 60	?
$f_1(1285)$	0^+1^+	25	$\rho\rho$	≤ 8	1.65
$\pi'(1300)$	1^-0^-	~ 400	$\rho\pi$	seen	?

Table 2 Mesonic Resonances R with masses $m_R \leq 1300$ MeV and substantial branching ratios into final states involving direct ρ's (hadronic) or ρ-like photons (radiative). Table taken from [68].

with the four-momenta p^μ, q^μ, and k^μ of the pseudoscalar, ρ, and vector or axial-vector meson, respectively. The ρP scattering through a vector-meson resonance is due to the Wess-Zumino anomaly.

Further the ρP scattering can also be mediated by a pseudoscalar resonance, $\rho\pi \to \pi'(1300)$ with the interaction Lagrangian

$$\mathscr{L}_{\rho P P'} = G_{\rho P P'} P'(k \cdot q p_\mu - p \cdot q k_\mu)\rho^\mu P. \tag{40}$$

Finally, there are $\rho V A$ vertices related to anomaly terms,

$$\mathscr{L}_{\rho V A} = G_{\rho V A} \epsilon_{\mu\nu\rho\sigma} p^\mu V^\nu \rho^{\rho\alpha} k_\alpha A^\sigma - \frac{\lambda}{2}(k_\beta A^\beta)^2, \tag{41}$$

with the field-strength tensor $\rho_{\mu\nu} = q_\mu \rho_\nu - q_\nu \rho_\mu$. The second term on the right-hand side is a gauge-fixing term for the axial-vector field, and the Feynman gauge is chosen by setting $\lambda = 1$.

The considered vector and axial-vector mesons as well as the heavy pseudoscalar $\pi'(1300)$ with their corresponding decay properties to ρh and γh partial decay widths are summarized in Table 2. These widths are calculated with the above defined interaction vertices, taking into account the finite width of the ρ meson. Additionally hadronic dipole-form factors,

$$F_{\rho P R}(q_{\rm cm}) = \left(\frac{2\Lambda^2_{\rho P} + m_R^2}{2\Lambda^2_{\rho P} + [\omega_\rho(q_{\rm cm}) + \omega_P(q_{\rm cm})]^2} \right)^2, \tag{42}$$

are introduced.

The medium modifications of the ρ-meson self-energy and the corresponding spectral function is then evaluated with these model parameters. As is nicely demonstrated in Fig. 7, any process adds to the imaginary part of the self-energy, i.e., the ρ-meson width, while the contribution to the real part around the vacuum mass can be positive or negative, depending on whether the effective interaction due to the involved meson resonances is repulsive or attractive, respectively. The net result is a considerable broadening of the ρ-meson's spectral shape with only moderate mass shifts. The same qualitative feature is also seen when taking all the in-medium effects on the ρ-meson self-energy into account, i.e., the modification of the pion cloud in the

R	$IF(\rho hR)$	$G_{\rho hR}$ (GeV^{-1})	$\Lambda_{\rho hR}$ (MeV)	$\Gamma^0_{\rho h}$ (MeV)	$\Gamma^0_{\gamma h}$ (MeV)
$\omega(782)$	1	25.8	1000	3.5	0.72
$h_1(1170)$	1	11.37	1000	300	0.60
$a_1(1260)$	2	13.27	1000	400	0.66
$K_1(1270)$	2	9.42	1000	60	0.32
$f_1(1285)$	1	35.7	800	3	1.67
$\pi'(1300)$	2	9.67	1000	300	0

Table 3 Results of the fit to the decay properties of ρ-h induced mesonic resonances R with masses $m_R \leq 1300$ MeV (the $f_1(1285)$ and $\pi'(1300)$ coupling constants are in units of GeV^{-2}). $IF(\rho hR)$ denotes the isospin factor in the decay-matrix element. Table taken from [68].

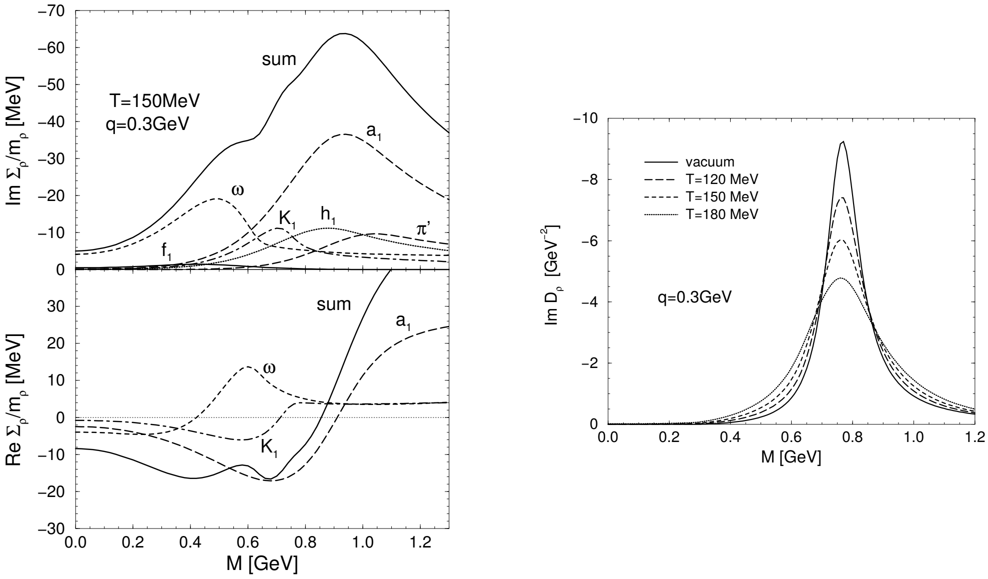

Fig. 7 The polarization-averaged in-medium ρ-meson self-energy (left) and spectral function (right). Figures taken from [68].

$\rho\pi\pi$ loop as well as the just discussed direct interactions of the ρ with mesonic and baryonic resonances, one finds a tremendous broadening of the spectral function with only small mass shifts [69]. It is important to note that the baryons provide a lot of spectral strength in the low-mass tail, which within the VMD model leads to a considerable enhancement of the dilepton-production rate down to the $\ell^+\ell^-$ threshold. As already shown in Fig. 5 the full in-medium dilepton-production rates close to the pseudo-critical temperature for the chiral phase transition, obtained by extrapolating the pertinent partonic rates down and the hadronic rates up to temperatures around $T_{\rm c} \simeq 160$ MeV become very similar, hinting at a restoration of chiral symmetry through "melting of the vector-meson resonances" merging smoothly into the corresponding QCD continuum.

In the intermediate-mass region, $m_\phi \lesssim M_{\ell^+\ell^-} \lesssim m_{J/\psi}$, medium modifications can be addressed approximately using a low-temperature/density expansion, leading to a mixing of the vector and axial-vector current-correlation functions via the presence of

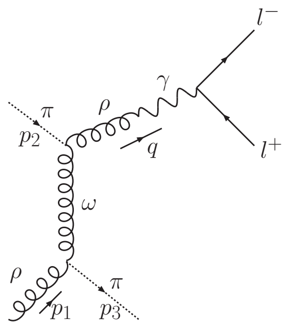

Fig. 8 Feynman diagram describing the annihilation of a ρ meson, $\rho\pi \to \pi\ell^+\ell^-$ via the t-channel exchange of an ω meson. Figure taken from [85].

thermal pions [83],

$$\begin{aligned}\Pi_V(q) &= (1-\epsilon)\Pi_V^{\text{vac}}(q) + \epsilon\Pi_A^{\text{vac}}(q),\\ \Pi_A(q) &= \epsilon\Pi_V^{\text{vac}}(q) + (1-\epsilon)\Pi_A^{\text{vac}}(q).\end{aligned} \tag{43}$$

The mixing coefficient ϵ is given by pion tadpole diagrams via a thermal loop integral,

$$\epsilon = \frac{2}{f_\pi^2}\int \frac{\mathrm{d}^3\vec{k}}{(2\pi)^3\omega_k^\pi} f_\pi(\omega_k^\pi; T), \tag{44}$$

where $\omega_k^\pi = \sqrt{m_\pi^2 + k^2}$ is the on-shell energy of the pion and $f_\pi = 93$ MeV the pion-decay constant. For $\epsilon \to 1/2$ this leads to a full restoration of chiral symmetry around $T = T_\mathrm{c} \simeq 160$ MeV, i.e., degeneracy in the vector and axial-vector correlation function. In the intermediate mass region this leads to a smooth distribution resembling the QCD continuum.

In [84, 85] this chiral-mixing effect is implemented taking into account the presence of an effective pion chemical potential, which ensures the conservation of the pion number after chemical freezeout (in Boltzmann approximation), using (43) with a mixing parameter $\hat{\epsilon} = \frac{1}{2}\epsilon(T,\mu_\pi)/\epsilon(T_\mathrm{c},0)$ and with a fugacity factor $z_\pi = \exp(\mu_\pi/T)$ in (44). Here it is important to avoid double counting with the above described in-medium evaluations of the ρ self-energy due to interactions with vector and axial-vector mesons, i.e., the two-pion piece and the part corresponding to the $a_1 \to \rho\pi$ decay have to be omitted. A detailed analysis, based on the chiral-reduction formalism [86, 87], finally leads to

$$\Pi_V = (1-\hat{\epsilon})z_\pi^4\Pi_{V,4\pi}^{\text{vac}} + \frac{\hat{\epsilon}}{2}z_\pi^3\Pi_{A,3\pi}^{\text{vac}} + \frac{\hat{\epsilon}}{2}(z_\pi^4 + z_\pi^5)\Pi_{A,5\pi}^{\text{vac}}. \tag{45}$$

As a further source of dileptons from a hot and dense hadronic medium, relevant at higher three-momenta, in [85] also contributions from the annihilation of a ρ meson through ω-meson t-channel exchange has been taken into account (cf. Fig. 8). The ρ-γ mixing vertex has been implemented by the Lagrangian $\mathscr{L}_{\rho\gamma} = -Cm_\rho^2 A_\mu\rho^\mu$, using the strict VMD value $C = e/g_{\rho\pi\pi} = 0.052$ [68]. For the intermediate ρ-meson line in Fig. 8 the full in-medium propagator of the ρ meson has been used, and for the incoming

ρ-meson line a weight $(-2m_\rho/\pi)\,\mathrm{Im}\,D_\rho(m_\rho)$. The coupling $g_{\rho\omega\pi} = 25.8\ \mathrm{GeV}^{-1}$ is fixed in [68] by a simultaneous fit to the hadronic and radiative ω decays, taking into account a hadronic dipole-form factor,

$$F(t) = \left(\frac{2\Lambda^2}{2\Lambda^2 - t}\right)^2 \tag{46}$$

with $\Lambda = 1$ GeV. To ensure gauge invariance, the form factor is taken out of the integral, introducing an average momentum transfer $\bar{t}$ via [88]

$$\begin{gathered} \frac{F^4(\bar{t})}{(m_\omega^2 - \bar{t})^2} = \frac{1}{2}\int_{-1}^{1} \mathrm{d}x \frac{F^4[t(x)]}{[m_\omega^2 - t(x)]^2}, \\ t(x) = M^2 + m_\pi^2 - 2(M^2 + q^2 - 2p \cdot qx). \end{gathered} \tag{47}$$

Finally, to avoid double counting with the s-channel ω-exchange contribution, which is already included in the evaluation of the in-medium ρ self-energy, in evaluating the corresponding dilepton-emission rate from standard kinetic theory the integral has been restricted to the kinematic region $t < 0$ (for details, see [85]).

For a realistic description of the dilepton production in heavy-ion collisions one has to take into account also non-thermal sources: ρ decay after thermal freeze-out as well as decay of high-momentum ρ mesons and Drell-Yan pairs produced in primordial hard collisions.

For the decay of ρ mesons after thermal freezeout the usual Cooper-Frye description [85],

$$\mathrm{d}N = q_\mu \mathrm{d}\sigma^\mu \frac{\mathrm{d}^3\vec{q}}{(2\pi)^3 q^0} f_{\mathrm{B}}\left(\frac{q_\mu u^\mu}{T}\right), \tag{48}$$

is used, where q_μ is the four-momentum of the particle, $\mathrm{d}\sigma^\mu$ a freezeout-surface element, and u^μ the local four-velocity of the fluid cell under consideration. To take into account the finite width of the ρ meson one uses the substitution

$$\frac{\mathrm{d}^3\vec{q}}{q^0} = \mathrm{d}^4q 2\Theta(q^0)\delta(q_\mu q^\mu - m^2) \rightarrow \mathrm{d}^4q \frac{A_\rho}{\pi}, \quad A_\rho = -\frac{2}{3}\,\mathrm{Im}(D_\rho)_\mu^\mu. \tag{49}$$

Within the VMD model the corresponding dilepton rate is given by the matrix element for the process $\rho \rightarrow \gamma^* \rightarrow \ell^+\ell^-$,

$$\frac{\mathrm{d}N_{\ell\ell}}{\mathrm{d}^3\vec{x}\mathrm{d}^4q} = \frac{\alpha_{\mathrm{em}}^2 m_\rho^4}{g_\rho^2 M^2} \frac{A_\rho}{2\pi^3} L(M) f_{\mathrm{B}}\left(\frac{q \cdot u}{T}\right) \frac{q^0}{M\Gamma_\rho^{(\mathrm{fo})}}, \tag{50}$$

where

$$L(M) = \left(1 + \frac{2m_\ell^2}{M^2}\right)\sqrt{1 - \frac{4m_\ell^2}{M^2}} \tag{51}$$

is the dilepton phase-space factor. One should note that compared to the emission from a thermal source the spectral shape is modified by the life-time dilation factor $\gamma = q^0/M = \sqrt{\vec{q}^2 + M^2}/M$.

To estimate the contribution to the dilepton rate from ρ mesons produced in hard initial collisions, which do not fully equilibrated with the bulk medium, one starts from a phenomenological q_{T} spectrum in pp collisions,

$$\frac{1}{q_{\mathrm{T}}}\frac{\mathrm{d}N_{\mathrm{prim}}}{\mathrm{d}q_{\mathrm{T}}} = \frac{A}{(1+Bq_{\mathrm{T}}^2)^a} \tag{52}$$

with $B = 0.525\ \mathrm{GeV}^{-2}$ and $a = 5.5$ from fitting pp-scattering data [89] (for 400 GeV pp collisions). The total number of primordial ρ mesons in AA collisions is estimated from the empirical freeze-out systematics of light-hadron production [85]. To take cold-nuclear matter effects into account the Cronin effect is implemented by a "Gaussian smearing" of the spectrum (52),

$$\frac{\mathrm{d}N_{\mathrm{prim}}^{\mathrm{cron}}}{\mathrm{d}^2 q_{\mathrm{T}}} = \int \frac{\mathrm{d}^2 q_{\mathrm{T}}}{\pi \Delta k_{\mathrm{T}}^2}\frac{\mathrm{d}N_{\mathrm{prim}}}{\mathrm{d}^2 k_{\mathrm{T}}} \exp\left[-\frac{(q_{\mathrm{T}}-k_{\mathrm{T}})^2}{\Delta k_{\mathrm{T}}^2}\right], \tag{53}$$

with $\Delta k_{\mathrm{T}}^2 = 0.2\ \mathrm{GeV}^2$ based on direct-photon spectra in pA collisions [88]. Finally the absorption of primordial ρ mesons through traversing the medium ("jet quenching") is evaluated by estimating the escape probability

$$P = \exp\left[-\int \mathrm{d}t \sigma_{\rho}^{\mathrm{abs}}(t)\varrho(t)\right], \tag{54}$$

where

$$\sigma_{\rho}^{\mathrm{abs}} = \begin{cases} \sigma_{\mathrm{ph}} = 0.4\ \mathrm{mb} & \text{for} \quad t < q_0/m_\rho \tau_{\mathrm{f}}, \\ \sigma_{\mathrm{had}} = 5\ \mathrm{mb} & \text{for} \quad t > q_0/m_\rho \tau_{\mathrm{f}}, \end{cases} \tag{55}$$

with the ρ-meson formation time $\tau_{\mathrm{f}} = 1$ fm; σ_{ph} and σ_{had} are the absorption cross sections for pre-hadrons and hadrons, respectively, and $\varrho(t)$ denotes the partonic or hadronic particle density of the medium.

Finally, the contribution to the dilepton yield from the Drell-Yan (DY) process, i.e., the quark-antiquark annihilation in hard initial collisions, is estimated using

$$\left.\frac{\mathrm{d}N_{\mathrm{DY}}^{AA}}{\mathrm{d}M\mathrm{d}y}\right|_{b=0} = \frac{3}{4\pi R_0^2} A^{4/3} \frac{\mathrm{d}\sigma_{\mathrm{DY}}^{NN}}{\mathrm{d}M\mathrm{d}y} \tag{56}$$

for central AA collisions with the root-mean squared radius $R_0 \simeq 1.05$ fm originating from folding over a Gaussian thickness function. The DY cross section in nucleon-nucleon collisions is given in leading order $\mathcal{O}(\alpha_{\mathrm{s}}^0 \alpha_{\mathrm{em}}^2)$ by

$$\frac{\mathrm{d}\sigma_{\mathrm{DY}}^{NN}}{\mathrm{d}M\mathrm{d}y} = K\frac{8\pi\alpha_{\mathrm{em}}}{9sM} \sum_{q=u,d,s} e_q^2 \left[q(x_1)\overline{q}(x_2) + \overline{q}(x_1)q(x_2)\right]. \tag{57}$$

where $q(x_{1,2})$ and $\overline{q}(x_{1,2})$ denote the GRV94LO parton-distribution functions for quarks and antiquarks [90]. The K factor takes into account higher-order corrections in

α_s with $K \simeq 1.5$ as inferred from data on DY production in pA collisions [91]. Higher-order effects also lead to a non-zero dilepton-q_T, which is adopted from the procedure by the NA50 Collaboration [92, 93], according to which in both pA and AA collisions the q_T dependence of the DY dileptons can be described by a Gaussian distribution,

$$\frac{dN_{DY}}{dM dy dq_T^2} = \frac{dN_{DY}}{dM dy} \frac{\exp(-q_T^2/2\sigma_{q_T}^2)}{2\sigma_{q_T}^2} \tag{58}$$

with $\sigma_{q_T} \simeq 0.8$-1 GeV.

The DY contribution in the region of low invariant mass and momentum, $M, q \lesssim 1.5$ GeV is problematic. In AA collisions it is small compared to the emission from thermal sources, but becomes significant at higher $q_T \gtrsim 1$ GeV. There the additional constraint by the photon point $M \to 0$ allows an extrapolation of the DY spectrum to lower mass [85]: Comparing the emission rate for dileptons from a thermal source (9) with that of photons we see that for $q \gg M$

$$q_0 \frac{dN_{\ell\ell}}{dM d^3\vec{q}} = q_0 \frac{dN_\gamma}{d^3\vec{q}} \frac{2\alpha_{em}}{3\pi M}. \tag{59}$$

Thus we evaluate the DY-q_T spectrum at a mass $M_{cut} = 0.8$-1 GeV and extrapolate it down in mass by M_{cut}/M.

Finally, for photon production in addition to the already discussed hadronic model for the in-medium electromagnetic current correlator, some additional meson-exchange reactions (π, K, ρ, K^*, and a_1) in a meson gas become relevant at photon momenta $q \gtrsim 1$ GeV [88]. Here a massive-Yang-Mills model based on a nonlinear $U_L(3) \times U_R(3)$-σ model has been employed:

$$\begin{aligned}\mathscr{L} =& \frac{1}{8} F_\pi^2 \mathrm{Tr} D_\mu U D^\mu U^\dagger + \frac{1}{8} F_\pi^2 \mathrm{Tr} M (U + U^\dagger - 2) \\ & - \tfrac{1}{2} \mathrm{Tr}\left(F_{\mu\nu}^L F^{L\mu\nu} + F_{\mu\nu}^R F^{R\mu\nu}\right) + m_0^2 \mathrm{Tr}\left(A_\mu^L A^{L\mu\nu} + A_\mu^R A^{R\mu}\right) + \gamma\, \mathrm{Tr}\, F_{\mu\nu}^L U F^{R\mu\nu} U^\dagger \\ & - i\xi\, \mathrm{Tr}\left(D_\mu U D_\nu U^\dagger F^{L\mu\nu} + D_\mu U^\dagger D_\nu U F^{R\mu\nu}\right) .\end{aligned} \tag{60}$$

Here

$$\begin{aligned} U &= \exp\left(\frac{2i}{F_\pi} \sum_i \frac{\phi_i \lambda_i}{\sqrt{2}}\right) = \exp\left(\frac{2i}{F_\pi}\phi\right) , \\ A_\mu^L &= \tfrac{1}{2}(V_\mu + A_\mu) , \\ A_\mu^R &= \tfrac{1}{2}(V_\mu - A_\mu) , \\ F_{\mu\nu}^{L,R} &= \partial_\mu A_\nu^{L,R} - \partial_\nu A_\mu^{L,R} - i g_0 \left[A_\mu^{L,R}, A_\nu^{L,R}\right] , \\ D_\mu U &= \partial_\mu U - i g_0 A_\mu^L U + i g_0 U A_\mu^R , \\ M &= \frac{2}{3}\left[m_K^2 + \frac{1}{2} m_\pi^2\right] - \frac{2}{\sqrt{3}}(m_K^2 - m_\pi^2)\lambda_8 \end{aligned} \tag{61}$$

with $F_\pi = 135$ MeV and the Gell-Mann matrices λ_i; ϕ, V_μ, and A_μ are the pseudoscalar, vector and axial-vector meson matrices, respectively.

In the non-strange sector, including pions, ρ, and a_1 mesons, in [94] two parameter sets for the four free parameters have been fitted to the masses and widths of the ρ and a_1 mesons,

$$\begin{aligned} I: \quad & \tilde{g} = 10.3063, \quad \gamma = 0.3405, \; \xi = 0.4473, \; m_0 = 0.6253\text{GeV}, \\ II: \quad & \tilde{g} = 6.4483, \quad \gamma = -0.2913, \; \xi = 0.0585, \; m_0 = 0.875\text{GeV}. \end{aligned} \tag{62}$$

In [95] the D- and S-wave content in the $a_1 \to \rho\pi$ decay has been found to be $D/S = 0.36$ and $D/S = -0.099$ for parameter sets I and II, respectively. Given the experimental finding of $D/S = -0.107 \pm 0.016$, in the following parameter set II has been used, employing the kinetic-theory expression for a photon-production process, $1 + 2 \to 3 + \gamma$,

$$\begin{aligned} q_0 \frac{\mathrm{d}R_\gamma}{\mathrm{d}^3\vec{q}} = \int & \frac{\mathrm{d}^3\vec{p}_1}{2(2\pi)^3 E_1} \frac{\mathrm{d}^3\vec{p}_2}{2(2\pi)^3 E_2} \frac{\mathrm{d}^3\vec{p}_3}{2(2\pi)^3 E_3} (2\pi)^4 \delta^{(4)}(p_1 + p_2 \to p_3 + q) \\ & \times |\mathcal{M}|^2 \, \frac{f(E_1) f(E_2)[1 \pm f(E_3)]}{2(2\pi)^3}. \end{aligned} \tag{63}$$

For the matrix elements, Born graphs in all possible s-, t-, and u-channels for reactions of the type $X + Y \to Z + \gamma$, $\rho \to Y + Z + \gamma$, and $K^* \to Y + Z + \gamma$, where for X, Y, and Z all combinations of ρ, π, K, and K* mesons allowed by the conservation of charge, isospin, strangeness, and G parity have been considered. In addition also the same model for ω-t-channel exchange has been used for photons as for dileptons (analogous to Fig. 8 with a real photon instead of a dilepton, $\ell^+\ell^-$ in the final state). At all vertices hadronic dipole form factors (46) have been employed, ensuring gauge invariance by the averaging procedure defined in (47).

One should note that the here described phenomenological model, which cocentrates on the vector-isovector channel (light vector mesons) to describe dilepton production in heavy-ion collisions, is compatible with chiral symmetry as is demonstrated in [96] by constructing the axial-vector channel via QCD and chiral (Weinberg) sum rules. This study clearly demonstrates that the “broadening-resonance scenario” following from the phenomenological model is compatible with chiral-symmetry restoration, i.e., the mass spectra of the vector and axial-vector curren-current correlation function become degenerate at a temperature of about 170 MeV (cf. Fig. 9).

3.3 Bulk-evolution models

To evaluate the dilepton spectra in relativistic heavy-ion collisions in addition to the above discussed models for the various dilepton sources a reliable description of the evolution of the hot and dense medium created in such collisions is necessary. In the here discussed work simple **thermal-fireball parameterizations** (“blast-wave” models) as well as **coarse-grained transport simulations** have been employed.

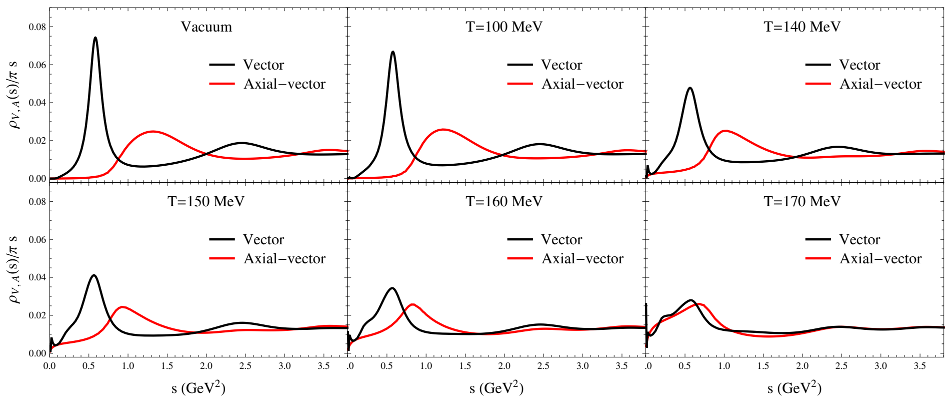

Fig. 9 The contruction of the axial-vector spectral function from the vector channel provided by the model for the in-medium spectral function of the ρ meson, demonstrating the compatibility of the resulting "broadening-mass scenario" for chiral-symmetry interpretaion. Figure taken from [96].

The thermal-fireball parameterizations are motivated by the observation that at the higher collision energies the bulk evolution of the medium is well-described by hydrodynamical expansion of a hot medium. In its simplest form the fireball volume is taken as an expanding cylinder with volume [69]

$$V_{\mathrm{FB}}(t) = \pi \left(r_{\perp,0} + \frac{1}{2} a_\perp t^2 \right)^2 \left(z_0 + v_{z,0} t + \frac{1}{2} a_z t^2 \right). \tag{64}$$

The initial transverse radius $r_{\perp,0}$ is determined by the centrality of the collision. The initial longitudinal size z_0 reflects the formation time $\tau_0 = 1$ fm$/c$ of the thermal medium, which translates into $z_0 \simeq \tau_0 \Delta y = 1.8$ fm, where $\Delta y = 1.8$ is the rapidity width of a thermal fireball. The values for the transverse acceleration are determined together with the fireball lifetime by the transverse-momentum spectra of hadrons, which are affected by the "Doppler blueshift" due to the radial flow. In accordance with hydrodynamical calculations the radial flow-velocity is assumed to grow linearly with $r_\perp$,

$$v_\perp(t, r_\perp) = \frac{r_\perp}{r_{\perp,0} + a_\perp t^2/2} a_\perp t. \tag{65}$$

With given expansion parameters, the fireball life-time is determined by the condition for thermal freeze-out which can also be determined from measurements of the hadronic spectra (see, e.g., for SPS energies [97–101]). The time evolution of the temperature is determined by the simplifying assumption that the temperature is constant throughout the fireball volume (i.e., taken as an average temperature) and that the expansion is isentropic in accordance with ideal hydrodynamics, using an EoS. For $T > T_{\mathrm{c}}$ an ideal partonic EoS and a hadron-resonance-gas (HRG) EoS for $T < T_{\mathrm{c}}$ has been used. In [84, 85] a first-order transition has been assumed, connecting the QGP and HRG phases with a mixed phase at $T = T_c = \text{const}$ with the hadron-gas fraction,

$$f_{\mathrm{HG}}(t) = \frac{s_c^{\mathrm{QGP}} - s(t)}{s_c^{\mathrm{QGP}} - s_c^{\mathrm{HG}}}. \tag{66}$$

Of course, also other EoS with a cross-over transition, which is more adequate at higher beam energies, like latPHG [102] can be easily implemented. After chemical freeze-out the system falls off chemical equilibrium, and besides the usual baryochemical potential, μ_{B}, chemical potentials like μ_π and μ_{K} are introduced to keep the particle abundances fixed. The chemical potential of resonances is then determined through their (finally stable) decay products; e.g., for the Δ resonance, decaying mostly into πN, $\mu_\Delta = \mu_{\mathrm{B}} + \mu_\pi$ or for the ρ meson $\mu_\rho = 2\mu_\pi$, etc.

To also take into account the elliptic flow of hadrons in order to address the resulting elliptic flow of photons, in [103, 104] an elliptic blast-wave description has been developed. Also the parameterization of the radial flow of the fireball boundary in (64) has been substituted by the corresponding relativistic motion of constant proper acceleration, i.e., the velocities and lengths of the major axes of the ellipse follow the time evolution

$$\begin{aligned} v_a(t) &= \frac{a_a t}{\sqrt{1+(a_a t)^2}}, \quad v_b(t) = \frac{a_b t}{\sqrt{1+(a_b t)^2}}, \\ a(t) &= a_0 + \frac{\sqrt{1+(a_a t)^2}-1}{a_a}, \quad b(t) = b_0 + \frac{\sqrt{1+(a_b t)^2}-1}{a_b}. \end{aligned} \tag{67}$$

To define the flow field, confocal elliptic coordinates,

$$\vec{x}_\perp = r_0(\sinh u \cos v, \cosh u \sin v) \tag{68}$$

are introduced to parameterize the ellipse at each time, t, and the radial-flow velocity field is parameterized as

$$\vec{v}_\perp = \frac{r}{r_{\max}}(v_b \cos v, v_a \sin v). \tag{69}$$

The accelerations a_a and a_b are chosen differently in the QGP and hadronic phases and determined such that the transverse-momentum spectra and elliptic flow of hadrons (in the low-p_T range) are well described. It is assumed that multi-strange hadrons (like, e.g., the ϕ meson) freeze out kinetically already at the phase transition, while the light hadrons freeze out at the nominal kinetic freezeout (see Fig. 10).

For smaller beam energies the description of the bulk evolution of the medium created in heavy-ion collisions becomes questionable, and transport simulations become more reliable. On the other hand, a fully self-consistent off-equilibrium treatment of the in-medium properties of hadrons, which is necessary for a successful description of dilepton and photon production in heavy-ion collisions, is very challenging. In [109–112] a **coarse-grained transport approach** has been developed. Here, the

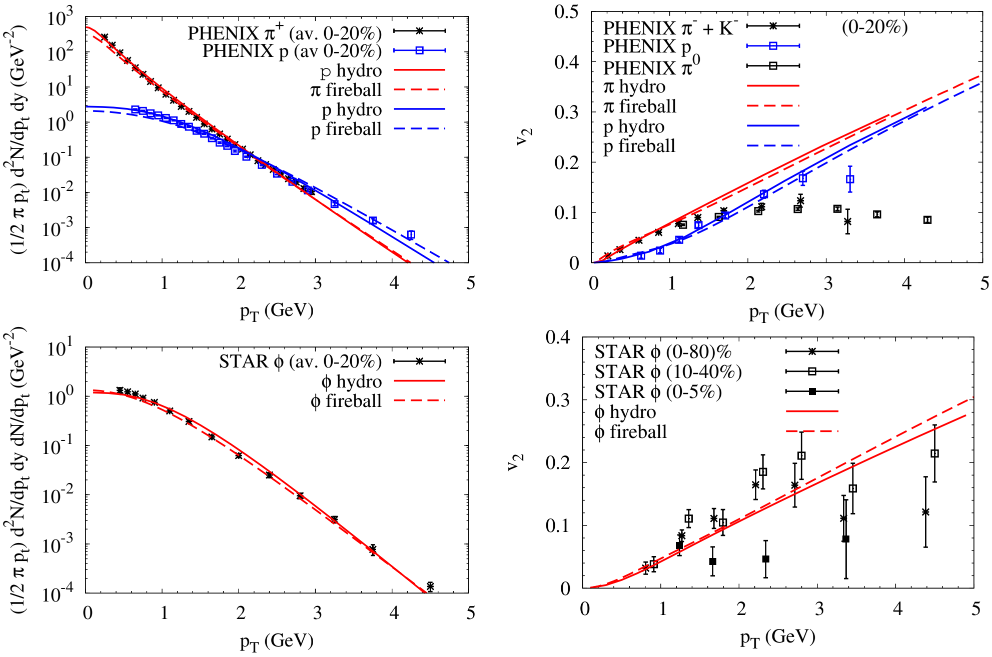

Fig. 10 Fits to the spectra and elliptic flow of light hadrons ($T_{\rm fo} \simeq 110$ MeV, upper two panels) and ϕ mesons ($T_{\rm fo} = 160$ MeV, lower two panels) in Au-Au($\sqrt{s} = 200$ AGeV) collisions, using EoS *latPHG* [102] within either the fireball (dashed lines) or ideal hydrodynamic model (solid lines). The data are taken from Refs. [105–108]. Figure taken from [104].

bulk evolution is simulated using the established transport simulation Ultrarelativistic Quantum Molecular Dynamics (UrQMD) [113–115]. Averaging over several runs, the phase-space distribution is mapped to a local equilibrium description within a space-time grid, using an appropriate EoS. In this way the thermal quantum-field theoretical results for the in-medium dilepton and photon production rates described above become applicable.

The grid of space-time cells is defined by $\Delta x = \Delta y = \Delta z = 0.7$-$0.8$ fm and $\Delta t = 0.2$-0.6 fm$/c$, and the energy-momentum tensor $T_{\mu\nu}$ and net-baryon four-flow $j_\mu^{\rm B}$ in each cell are evaluated via

$$\begin{aligned} T^{\mu\nu} &= \int \mathrm{d}^3p \frac{p^\mu p^\nu}{p^0} f(\vec{x},\vec{p},t) = \frac{1}{\Delta V} \left\langle \sum_{i=1}^{N_h \in \Delta V} \frac{p_i^\mu \cdot p_i^\nu}{p_i^0} \right\rangle, \\ j_{\rm B}^\mu &= \int \mathrm{d}^3p \frac{p^\mu}{p^0} f_{\rm B}(\vec{x},\vec{p},t) = \frac{1}{\Delta V} \left\langle \sum_{i=1}^{N_{\rm B/\overline{B}} \in \Delta V} \pm \frac{p_i^\mu}{p_i^0} \right\rangle, \end{aligned} \tag{70}$$

where the averaging is understood as averaging over several UrQMD events. The four-velocity of the fluid cell is defined using the Eckart definition, i.e., according to the

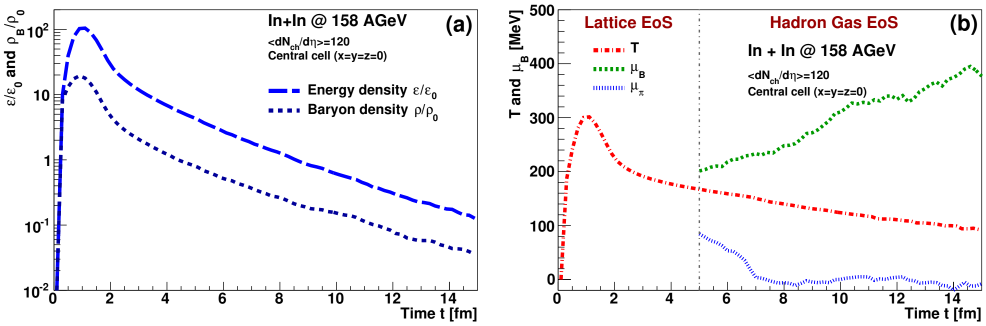

Fig. 11 Left panel: Time evolution of the baryon density $\rho_{\rm B}$ (short dashed) and energy density ε (long dashed) for the cell at the center of the coarse-graining grid ($x = y = z = 0$). The results are given in units of the ground-state densities ε_0 and ρ_0. Right panel: Time evolution of the temperature T (red dash-dotted), baryon chemical potential $\mu_{\rm B}$ (green short dashed) and the pion chemical potential μ_π (blue dotted) in the central cell. The thin grey line indicates the transition from the Lattice EoS to the Hadron Gas EoS at the transition temperature of $T = 170$ MeV. Figure taken from [109].

flow of the net-baryon number,

$$u^\mu = \frac{j^\mu_{\rm B}}{\sqrt{j_{\rm B} \cdot j_{\rm B}}} = (\gamma, \gamma\vec{v}). \tag{71}$$

The transport simulations show that the assumption of isotropic thermal equilibrium in the fluid cells is not justified in the early stages of the collision. This kinetic off-equilibrium situation leads to the ansatz for the energy-momentum stress tensor within the anisotropic hydrodynamics approach [116–118],

$$T^{\mu\nu} = (\varepsilon + P_\perp)\, u^\mu u^\nu - P_\perp\, \eta^{\mu\nu} - (P_\perp - P_\parallel) v^\mu v^\nu, \tag{72}$$

where ε is the energy density, $P_\perp$ and $P_\parallel$ the pressures perpendicular and parallel to the beam direction; u^μ is the four-velocity of the fluid cell, and v^μ the four-vector of the beam direction. Then an effective energy density is obtained by the generalized EoS of a Boltzmann-like system via

$$\varepsilon_{\rm eff} = \frac{\varepsilon}{r(x)} \tag{73}$$

with the relaxation function

$$r(x) = \begin{cases} \frac{x^{-1/3}}{2}\left(1 + \frac{x\,\mathrm{artanh}\sqrt{1-x}}{\sqrt{1-x}}\right) & \text{for } x \le 1 \\ \frac{x^{-1/3}}{2}\left(1 + \frac{x\,\arctan\sqrt{x-1}}{\sqrt{x-1}}\right) & \text{for } x \ge 1 \end{cases}, \qquad x = \left(\frac{P_\parallel}{P_\perp}\right)^{3/4}. \tag{74}$$

It turns out that $\varepsilon_{\rm eff}$ deviates from the nominal energy density,

$$\varepsilon = u_\mu u_\nu T^{\mu\nu}, \tag{75}$$

only in the first 1-2 fm/c of the time evolution, where the pressure anisotropy is large. The effective energy density and net-baryon density are used to determine the temperature and baryochemical potential as well as the pion and kaon chemical potentials to take into account chemical off-equilibrium, matching the EoS in the QGP phase based on lattice calculations [102] with a hadron-resonance-gas EoS including the hadronic degrees of freedom implemented in UrQMD [119, 120] based on a hadronic chiral model [121, 122]. As an example Fig. 11 shows the time evolution of the net-baryon density, temperature, μ_{B}, and μ_{π} for the central cell of the medium created in 158 AGeV In-In collisions at the CERN SPS, as investigated in the NA60 experiment.

Another transport model used to describe dilepton production in heavy-ion collisions is Parton-Hadron-String Dynamics (PHSD) [123–125]. In the partonic phase it uses the dynamical quasiparticle model (DQPM) [126] to describe the transport of broad and massive quarks and gluons in the medium. Dilepton production is implemented using the processes $q\overline{q} \rightarrow \gamma^*$ (quark annihilation) $q+g \rightarrow q+\gamma^*$, $\overline{q}+g \rightarrow \overline{q}+\gamma^*$ (gluo-Compton scattering), and $q\overline{q} \rightarrow \gamma^* + g$ (gluon bremsstrahlung). In the hadronic phase the (off-shell) transport model is identical with the hadron-string-dynamics model (HSD) [127–130]. The dilepton sources include π-, η-, η', ω, Δ, a_1-Dalitz as well as $\rho, \omega, \phi \rightarrow \mathrm{e}^+\mathrm{e}^-$ decays.

4 Dilepton production at various beam energies

In this Section the results of simulations for heavy-ion collisions at various beam energies is summarized. All calculations are based on the microscopic models for dilepton production described in Sects. 3.1 and 3.2 for the emission from a QGP and a hot and dense hadron gas in the deconfined and confined phases of the evolution of the medium using the models discussed in Sect. 3.3.

4.1 Dielectron production at GSI-SIS energies

In [111] the production of dielectrons in heavy-ion collisions at GSI-SIS energies as measured by the HADES collaboration has been simulated using the coarse-grained transport approach as described in Sect. 3.3. An ensemble of 1000 UrQMD events has been used to obtain sufficient statistics, particularly for the contributions from non-thermal ρ and ω mesons. The impact-parameter distribution has been adapted to the HADES trigger conditions for Ar+KCl reactions at a beam energy of 1.76 AGeV [132] and Au+Au collisions at 1.23 AGeV [133, 134], using a Woods-Saxon-type fit, which in both cases approximately corresponds to a selection of the 0-40% most central collisions. For the Ar+KCl case, the number of neutral pions per event, used for the normalization of the spectra $N_{\pi^0}^{\mathrm{sim}} \simeq 3.9$ agrees well with the experimental finding, $N_{\pi_0}^{\mathrm{exp}} \simeq 3.5$. For the Au+Au collisions the simulation predicts $N_{\pi_0}^{\mathrm{sim}} \simeq 8.0$. In the simulation the overall normalization of the dilepton yield uses the simulated π_0 yields. To compare the simulated spectra with the experimental result the HADES acceptance filter [135] as well as the appropriate momentum cuts have been employed. To also confront the model with the data from the DLS collaboration on Ca+Ca collisions at a beam energy of 1.04 AGeV the DLS acceptance filter (version 4.1) [136] is used as well as an RMS smearing of 10% to account for the detector resolution. In this case

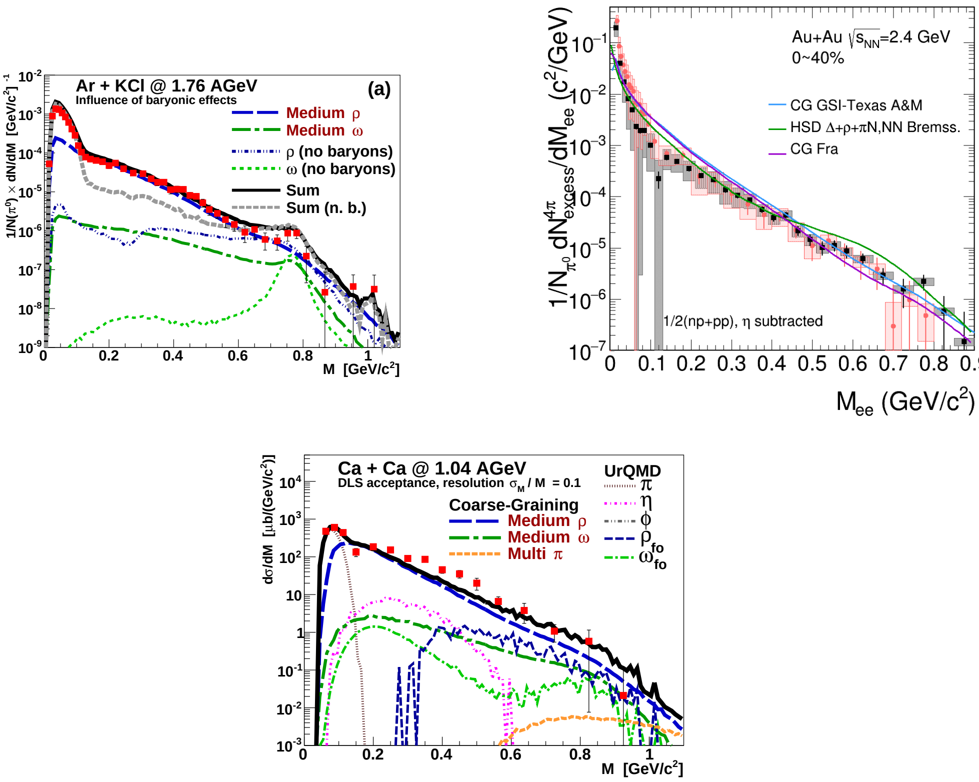

Fig. 12 Upper panels: Comparison of invariant mass spectra with the full spectral function and for the case of no baryonic effects (i.e., for $\rho_{\rm eff} = 0$). The dielectron yields for Ar+KCl collisions at $E_{\rm lab} = 1.76\ A$GeV (a) and for Au+Au at $E_{\rm lab} = 1.23\ A$GeV (b) are shown within HADES acceptance and normalized to the average number of produced π^0. Note that the UrQMD contributions are included in the sum, but the different single yields are not shown explicitly for reasons of lucidity. Lower panel: Invariant-mass spectrum of the dielectron yield for Ca+Ca collisions at $E_{\rm lab} = 1.04\ A$GeV within the experimental acceptance. The result is compared to the data from the DLS Collaboration [131]. Figures taken from [111].

a minimum-bias simulation has been employed since for DLS no impact-parameter distributions are available. The final invariant-mass spectrum is normalized to the total cross section of a Ca+Ca reaction.

In Fig. 12 the results for dielectron production in Ar+KCl collisions are compared to the data from the HADES collaboration and predictions for Au+Au collisions within the HADES acceptance are made. The observed enhancement of dileptons over the "hadronic cocktail" is well explained by the medium modifications of the ρ and ω meson. To underline the importance of the baryonic medium the calculation has also been performed neglecting ρ- and ω-baryon interactions. In addition also contributions from the decays of ρ- and ω-mesons in "non-thermal cells" (i.e., for cells of the space-time grid, for which a temperature $T < 50$ MeV results from the coarse-graining procedure) are included. Here the microscopic transport-theoretical cross sections as implemented in UrQMD are used (for details, see [111]).

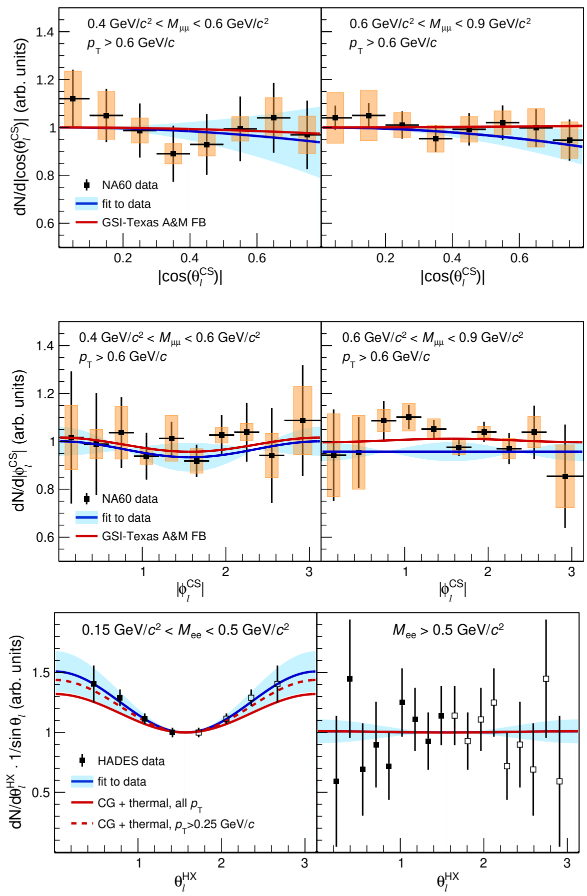

Fig. 13 Upper two rows: Dimuon angular distribution in the Colins-Soper frame calculated employing a coarse-graining approach using UrQMD simulations of the fireball evolution for implementing the in-medium thermal dilepton rates as described in [41] in comparison to NA60 data in 158A GeV In+In collisions [137]. The blue lines represent fits by NA60 with extracted anisotropy parameters of λ_θ= -0.10 $\pm$ 0.24 (upper left) and -0.13 $\pm$ 0.12 (upper right), compared to the calculated values of -0.04 and 0.01, respectively, and likewise λ_ϕ=0.05 $\pm$ 0.09 (lower left) and 0.00 $\pm$ 0.06 (lower right), compared to 0.04 and -0.01 from the calculation [41]. Last row: Comparison of calculated angular distributions (red lines) as defined in the helicity frame, integrated over two dielectron mass bins [41], to HADES data in Ar(1.76 GeV)+KCl collisions [138]. Fits by the HADES collaboration (blue lines with bands) yield anisotropy parameters of λ_θ=0.51 $\pm$ 0.17 (left panel) and 0.01 $\pm$ 0.1 (right panel) for the lower and higher mass window, respectively, compared to 0.34 and 0.01 from the calcuations. To illustrate effects of a finite HADES acceptance, theoretical results with a cut on transverse pair momentum in the lab of p_T>0.25 GeV are also shown (dashed red line).

More recently in addition also first assessments of the polarization of the dilepton pairs in both experiment [137, 139] and theory [41] has been achieved (cf. the last line of Fig. 13). This probes the difference between the transverse and longitudinal components of the in-medium current-correlation function, which has some sensitivity to the underlying in-medium scattering processes.

In [140] the elliptic flow, v_2 of di-electrons at HADES energies is investigated with the hadronic transport model SMASH [141]. First measurements of the HADES collaboration show $v_2^{(\mathrm{e}^+\mathrm{e}^-)} \simeq 0$ (except in the very low-mass region, where the dileptons dominately origin from pion-Dalitz decays and thus follow the negative v_2 of the pions, which is due to "squeeze-out") [142, 143]. In [140] it is shown that the "null result" of the HADES experiment is due to the cancellation of the v_2 of dileptons from different, competing hadronic sources, and this can be empirically validated by using the "tagging method" to determine the dilepton-elliptic flow, using the cross correlation of the event-flow vector of a specific particle species X,

$$q_n^X(\Omega) = \frac{\int_\Omega \mathrm{d}\Omega \int_0^{2\pi} \mathrm{d}\phi \frac{\mathrm{d}N^X}{\mathrm{d}\Omega \mathrm{d}\phi} \exp(\mathrm{i}n\phi)}{\int_\Omega \mathrm{d}\Omega \int_0^{2\pi} \mathrm{d}\phi \frac{\mathrm{d}N^X}{\mathrm{d}\Omega \mathrm{d}\phi}}, \tag{76}$$

and the corresponding quantity for the dileptons,

$$v_n^{(\mathrm{e}^+\mathrm{e}^-)}\{\mathrm{EP}|h\}(\Omega) = \mathrm{Cov}[q_n^{\mathrm{e}^+\mathrm{e}^-}(\Omega), q_n^h(\Omega)/|q_n^h(\Omega)|], \tag{77}$$

the socalled scalar-product flow. Using different hadron species, h, for "tagging" it might be possible to distinguish the varying v_n of dileptons depending on their origin from different hadronic sources (see Fig. 14).

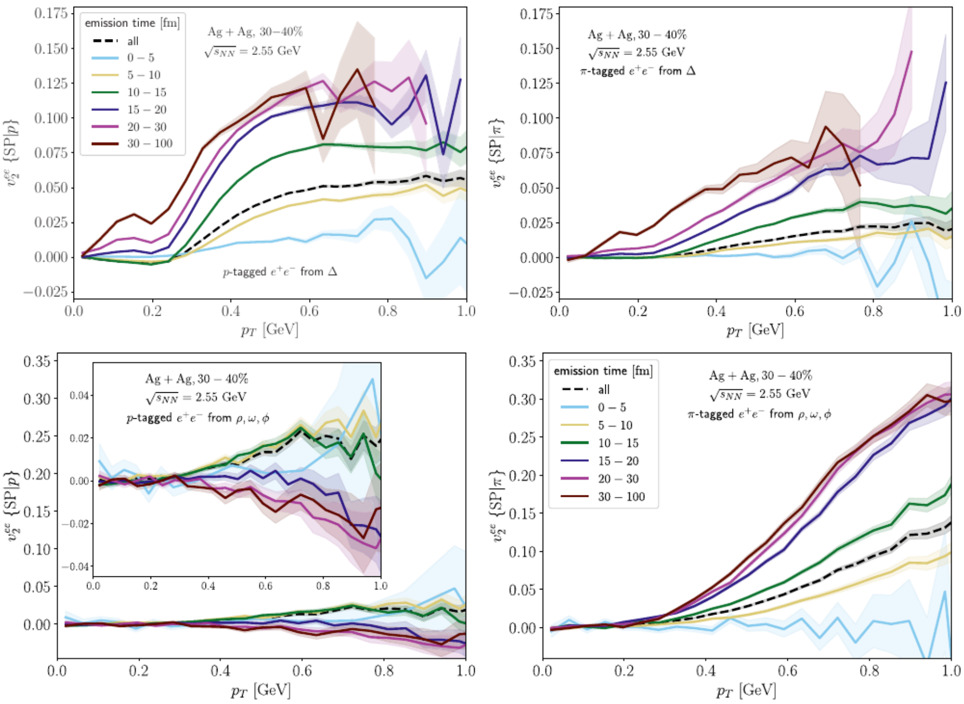

Fig. 14 Scalar product flow of dielectrons radiated by (upper) Δ baryons (upper panel) and vector mesons (lower panel). Solid lines show the flow signal at different time intervals, and the dashed-black lines show the full time integrated contribution of the source. The reference plane is constructed with (left) protons or (right) pions. Figure taken from [140].

4.2 Dimuon production at top CERN-SPS energy

In [84, 85] and [109] the dimuon production in 158 AGeV In-In collisions as measured by the NA60 collaboration [144–146, 148–150] at the CERN SPS have been calculated. To describe the medium evolution both blast-wave parameterizations and the coarse-grained transport approach have been applied.

As shown in Fig. 15 both descriptions of the fireball evolution lead to an excellent description of the data. It is important to note that here the hadronic cocktail has been subtracted from the data by the NA60 collaboration, i.e., a fully acceptance corrected *excess* spectrum is shown. Also the contribution from decays of correlated D and $\overline{\mathrm{D}}$ mesons and, for invariant masses $M_{\mu^+\mu^-} > 1.2$ GeV, Drell-Yan processes is subtracted. In the low-mass region $2m_\mu < M_{\mu^+\mu^-} \lesssim 1$ GeV the dominant contribution to the excess yield is from the decay of the tremendously broadened ρ mesons from the "thermal" medium, while at higher masses the contribution from the QGP is the leading contribution. Again the importance of the medium modifications becomes evident by comparing the full result to the case, where the baryon contributions to the ρ-meson self-energy are neglected. Particularly the enhancement in the very-low-mass region towards the two-muon threshold is mostly due to the interactions of the ρ meson with baryons (and anti-baryons), i.e., due to Dalitz decays of baryon

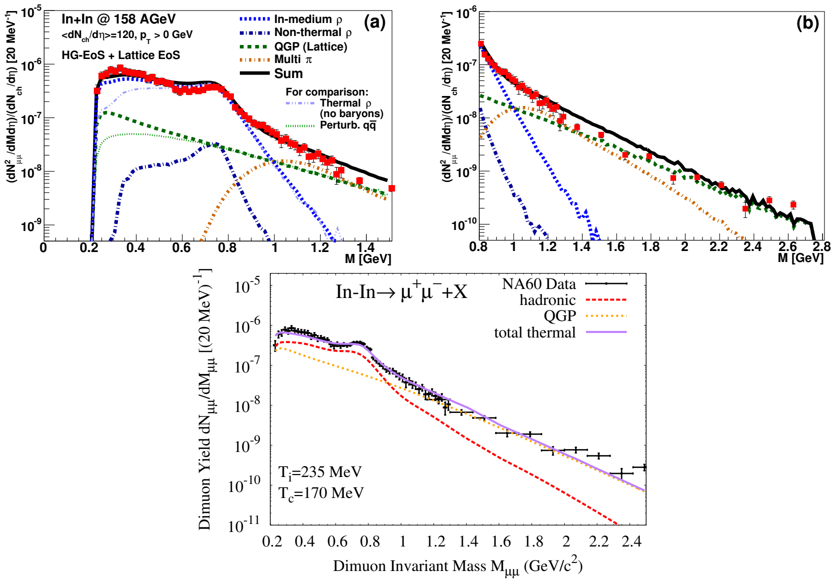

Fig. 15 Upper panels: Invariant mass spectra of the dimuon excess yield in In+In collisions at a beam energy of 158 AGeV, for the low-mass region up 1.5 GeV (a) and the intermediate-mass regime up to 2.8 GeV (b) using the coarse-grained transport description of the medium. We show the contributions of the in-medium ρ emission (blue short dashed), the contribution from the Quark-Gluon Plasma, i.e., $q\bar{q}$-annihilation, according to lattice rates [57, 60] (green dashed) and the emission from multi-pion reactions (orange dash-dotted). Additionally a non-thermal transport contribution for the ρ is included in the yield (dark blue dash-dotted). Only left plot: For comparison the thermal ρ without any baryonic effects, i.e. for $\rho_{\mathrm{eff}} = 0$, is shown (violet dash-double-dotted) together with the yield from pure perturbative $q\bar{q}$-annihilation rates (green dotted). The results are compared to the experimental data from the NA60 Collaboration [144–146]. Figures taken from [109]. Lower panel: The same model for the dimuon-production rates, using the blast-wave-fireball parameterization for the medium evolution. Figures taken from [147]).

resonances, which are included in the thermal quantum-field theoretical evaluation of the in-medium ρ-self-energy. As shown in [109] the model also successfully describes the q_{t} dependence as well as the mass spectra in various q_{t} bins. It should also be noted that in the invariant-mass region $m_\phi \lesssim M_{\mu^+\mu^-} \lesssim M_{J/\psi}$ after the above mentioned subtraction of contributions from decays of correlated D-$\overline{\mathrm{D}}$ pairs and the Drell-Yan process, a basically purely thermal contribution from the resonance-free region of the dilepton emission allows a direct determination of the space-time weighted average of the temperature. In this intermediate-mass region ($T \ll M_{\mu^+\mu^-}$) the emission from the earlier hot stages of the fireball evolution dominates, as is also reflected in the model calculation which identifies the thermal emission from the QGP as the main source. Indeed, a fit of the experimental data leads to a temperature $T = 205 \pm 12$ MeV [145], in accordance with the model.

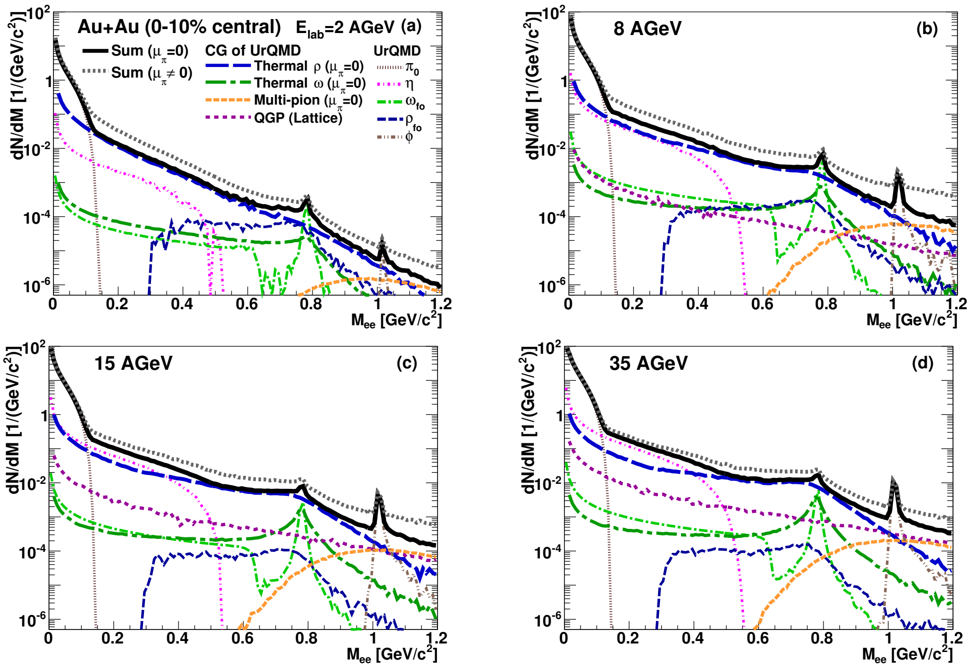

Fig. 16 Dilepton invariant mass spectra for Au+Au reactions at different energies $E_{\mathrm{lab}} = 2$-35 AGeV within the centrality class of 0-10% most central collisions. The resulting spectra include thermal contributions from the coarse-graining of the microscopic simulations (CG of UrQMD) and the non-thermal contributions directly extracted from the transport calculations (UrQMD). The hadronic thermal contributions are only shown for vanishing pion chemical potential, while the total yield is plotted for both cases, $\mu_\pi = 0$ and $\mu_\pi \neq 0$. Figure taken from [110]

4.3 Dileptons at FAIR and RHIC-BES energies

With the motivation to find possible signatures of the various phase transitions in the phase diagram of strongly interacting matter a beam-energy scan (BES) program is ongoing at RHIC and is also planned by the Compressed Baryonic Matter (CBM) experiment at the upcoming Facility for Antiproton and Ion Research (FAIR). In [110] we have thus evaluated the invariant-mass spectra for the four beam energies, $E_{\mathrm{lab}} = 2,\ 8,\ 15$ and 35 AGeV within the coarse-grained transport approach.

Since particularly at the lower beam energies the pion-chemical potential becomes quite large in the coarse-graining approach, we study its influence on the dilepton yield by using lower and upper boundaries with the following arguments: The lower bound is simply given by assuming $\mu_\pi = 0$. For the upper bound it should be noted that μ_π is an effective description for the off-chemical equilibrium nature of the medium, and thus in the here used Boltzmann approximation, its influence on the dilepton-production rate is given by a fugacity factor

$$z_\pi^n = \exp\left(\frac{n\mu_\pi}{T}\right), \tag{78}$$

where n is the difference in the number of pions in the initial and final state of the corresponding reaction process. For processes involving the ρ meson, particularly dilepton production in the here employed VMD model, not only two-pion production $\pi\pi \to \rho$ is relevant but, particularly at lower beam energies, baryonic channels like $\pi N \to N^*/\Delta \to \rho$ become important, for which $n < 2$. Thus, to estimate an upper limit of the influence of the pion chemical potential on the dilepton yield, we use $n = 2$ in our calculations.

As can be seen in Fig. 16, at all beam energies in the very-low-mass region, $M_{e^+e^-} < 0.15$ GeV, the dilepton yield is dominated by the Dalitz decays of neutral pions, $\pi^0 \to \gamma e^+e^-$, while beyond that region up to the vacuum-pole mass of the ρ meson of 770 MeV the main contribution is radiation from thermal sources with medium-modified ρ- and ω-meson spectral functions. Although the absolute yield of the thermal component increases with E_{lab}, its relative weight compared to the non-thermal η-Dalitz component and thus the enhancement above the hadronic cocktail contribution decreases.

Concerning the onset of deconfinement the calculations show that temperatures $T \simeq 170$ GeV are reached in the region of $E_{\text{lab}} = 6\text{-}8\ A\text{GeV}$.

Note that here we use the same cross-over-transition EoS for the coarse-graining procedure as for the higher beam energies. A possible deviation of the dilepton spectra from these predictions might thus indicate a possible change in the nature of the confinement-deconfinement and/or chiral phase transition.

Recently a comprehensive analysis of dielectron measurements by the STAR collaboration within the beam-energy-scan program (BES II) at RHIC has become available [151]. The measured acceptance corrected access yield are well compatible with models of the type described above. This is illustrated in Fig. 17.

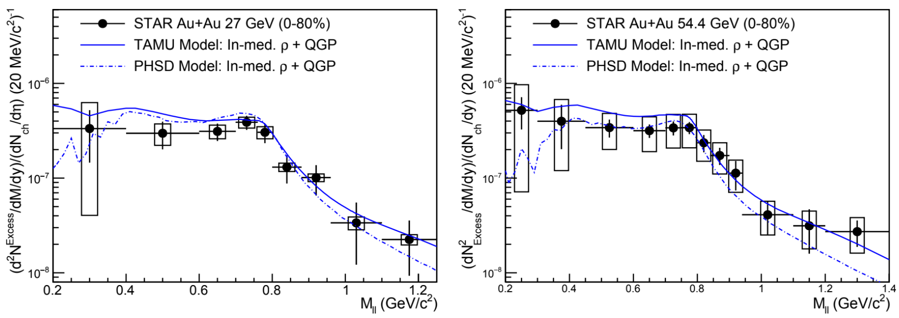

Fig. 17 Low mass excess dielectron invariant mass spectrum for Au+Au collisions at $\sqrt{s_{NN}} = 27$ GeV (left) and 54.4 GeV (right), normalized by $\mathrm{d}N_{\text{ch}}/\mathrm{d}y$, compared to the theoretical calculations from the TAMU [84, 147, 152] and PHSD [129, 153] models. Vertical bars and boxes around data points represent the statistical and systematic uncertainties, respectively. Figure taken from [151].

4.4 Dileptons at RHIC and LHC energies

In [112] we have employed the coarse-grained transport approach to the evaluation of dilepton spectra at RHIC and LHC energies. In Fig. 18 the result is shown

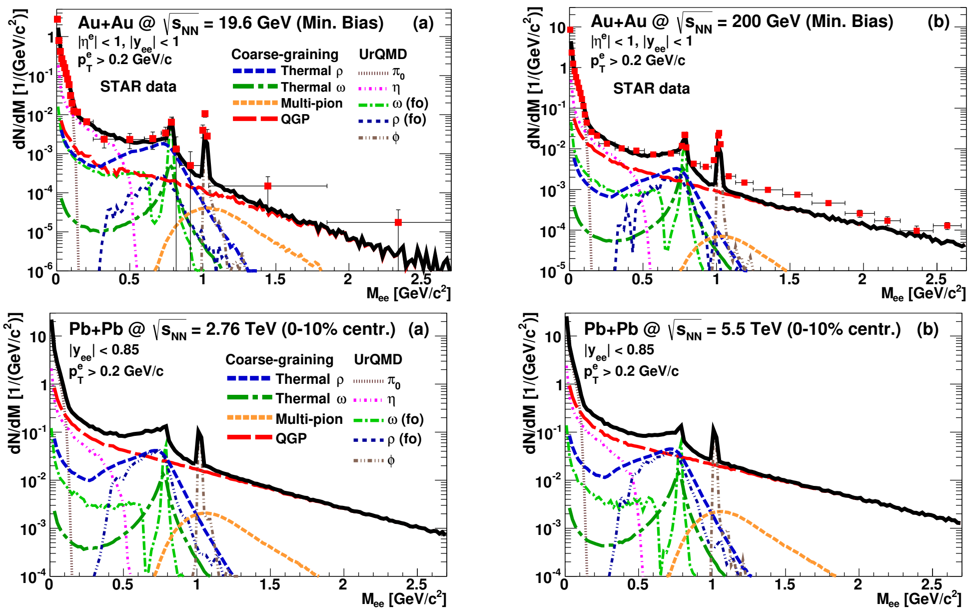

Fig. 18 Upper panel: Dielectron invariant-mass spectra for minimum bias (i.e., 0-80% most central) Au+Au collisions at $\sqrt{s_{NN}} = 19.6$ GeV (a) and 200 GeV (b). The sum includes the thermal hadronic and partonic emission obtained with the coarse-graining procedure, and also the hadronic π-, η- and ϕ-decay contributions from UrQMD as well as the "freeze-out" contributions (from cold cells) of the ρ and ω mesons. The model results are compared to experimental data obtained by the STAR Collaboration [154]. **Lower panel:** Dielectron invariant-mass spectra for 0-10% most central Pb+Pb collisions at $\sqrt{s_{NN}} = 2.76$ TeV (a) and 5.5 TeV (b). The sum includes the thermal hadronic and partonic emission obtained with the coarse-graining approach, and also the hadronic π, η, and ϕ decay contributions from UrQMD as well as the "freeze-out" contributions (from cold cells) of the ρ and ω mesons. Figures taken from [112]

.

in comparison to experimental data on Au-Au collisions at the two beam energies $\sqrt{s_{NN}} = 19.6$ GeV and 200 GeV [154]. The calculation takes into account the single-electron rapidity, the dielectron pseudorapidity, and transverse-momentum electron cuts ($\eta_{\mathrm{e}} < 1$, $y_{\mathrm{e}} < 1$, $p_t^{\mathrm{e}} > 0.2$ GeV) to account for the STAR acceptance. For the low-mass region, $M_{\mathrm{e^+e^-}} < 1$ GeV the data are well described within the model. In the region 0.3 GeV $< M_{\mathrm{e^+e^-}} <$ 0.7 GeV an access above the hadronic cocktail has been observed, and within our model at the lower beam energy this region is dominated by thermal contributions from medium-modified ρ mesons, while at top RHIC energy the emission from the QGP prevails. In both cases the spectral function of the in-medium ρ meson shows more similarities with its vacuum shape than at the lower beam energies discussed in the previous sections. This is understandable by the fact that here the baryon-chemical potential μ_{B} is smaller than at lower beam energies, and a great part of the broadening in the peak region as well as the low-mass tail is mainly due to the baryon interactions of the ρ meson, as already emphasized before. At intermediate masses $M_{\mathrm{e^+e^-}} > 1$ GeV our calculation underestimates the measured yield, which can be explained by the fact that here the contributions from Drell-Yan processes as well as decays of correlated $D\overline{D}$ mesons have been neglected. For further details on the comparison of the model on the data, see [112].

Also in Fig. 18 we present our predictions for Pb-Pb collisions at center-mass energies, available at the LHC, $\sqrt{s_{NN}} = 2.76$ TeV and 5.5 TeV. As to be expected also here the thermal ρ contribution in the low-mass region shows the vacuum-like peak structure as already seen at the lower RHIC energies; again this is due to the even smaller baryochemical potential at the higher beam energies. Compared to RHIC energies the fireball at LHC energies starts with considerable higher temperatures, leading to larger lifetimes for both the partonic and hadronic phase of the fireball evolution, resulting in larger contributions from both the QGP and the thermal vector mesons in the low-mass region.

More recently a detailed study based on calculations of the dilepton production in the pre-equilibrium stage of the fireball evolution as well as thermal partonic dilepton rates at next-to-leading (NLO) perturbative-QCD order in α_{s} [155, 156] including dilepton spectra, anisotropic flow coefficients, and polarization observables at LHC energies has been achieved in [43, 157, 158]. Here the fireball evolution has been described in a multi-stage model: the initial state is described, using the IP-Glasma [159, 160] and KØMPØST [161, 162] models as described in [163]. The corresponding dilepton rate is estimated by determining a quasi-hydrodynamic description in terms of a local temperature and fluid velocity of the off-equilibrium medium by Landau matching with the HotQCD Equation of State. Since the IP-Glasma and KØMPØST assume a purely gluonic initial states and the dileptons can only occur from the charged quarks, which build up in processes like $gg \rightarrow \mathrm{e}^+\mathrm{e}^-$ during the pre-equilibrium fireball evolution, an effective suppression factor is implemented. After a fixed formation time $\tau_0^{(\mathrm{hydro})} = 0.8\,\mathrm{fm}/c$ is decribed by the IBE-MUSIC hydrodynamic simulation [164–166] with the same thermal dilepton rates as used for the pre-equilibrium stage.

The hydrodynamic evolution ends by freezing out if a fluid cell's energy density drops below $\epsilon_{frz} = 0.18\,\mathrm{GeV}/\mathrm{fm}^3$ using the Cooper-Frye description taking into account viscous effects [167–169] followed by a hadronic UrQMD afterburner [170].

As illustrative examples for the results of this comprehensive model we depict in Fig. 19 the invariant mass spectrum (left), which sholws the sensitivity of the dilepton yield to off-equilibrium ("non-thermel") contributions, and the polarization coefficient λ_θ in the HX frame, underlining the sensititivity of the polarization observables to NLO pQCD contributions.

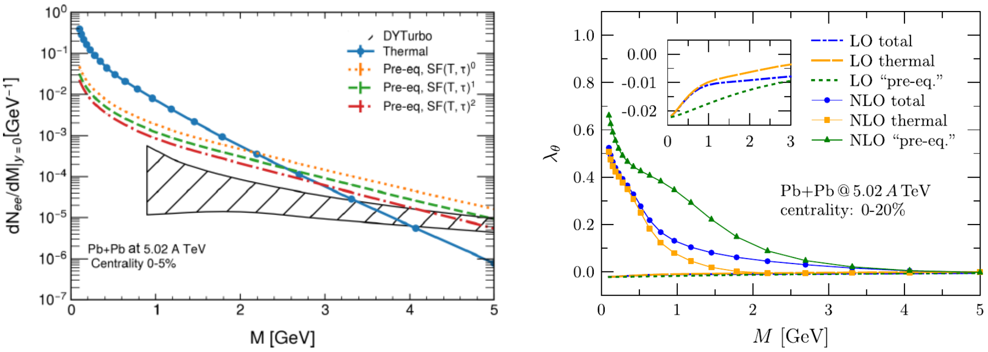

Fig. 19 Left panel: The thermal dilepton-invariant mass spectrum in comparison to the off-equilibrium distribution including the effective suppression factor (0: none, 1: linear, 2: squared) as well as the contribution from the Drell-Yan processes employing the DYTURBO package [171]. Figure taken from [157]. Right panel: The polarization coefficient λ_θ in the HX frame. Figure taken from [158].

Recently the ALICE collaboration has measured dielectrons at the LHC in Pb-Pb collisions at $s_{NN} = 5.02\,\text{TeV}$ [172]. As illustrated in Fig. 20 the excess yield is in accordance with the Rapp-Wambach as well as with the PHSD models. It is notable that for the first time the "distances of closest approach" method has been employed to subtract possible (thermal) contributions of dileptons from correlated D$\overline{D}$ decays in the IMR ($1.2\,\text{GeV} < M_{\mathrm{e}^+\mathrm{e}^-} < 2.6\,\text{GeV}$).

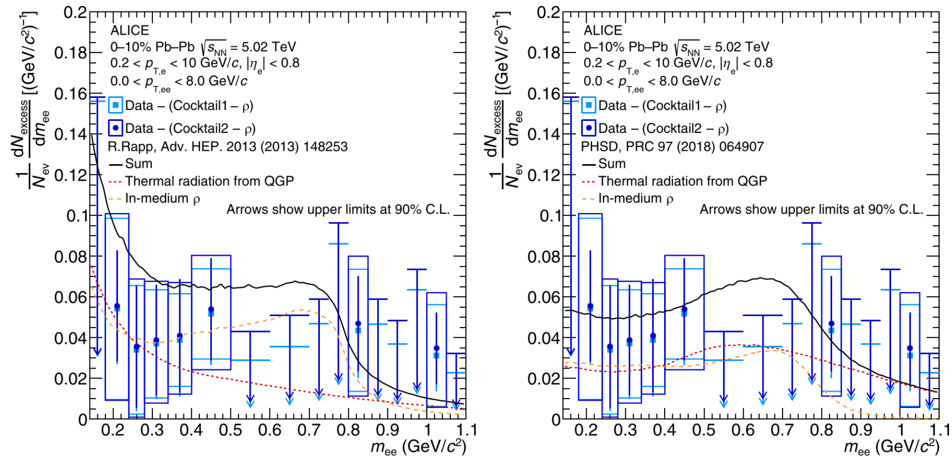

Fig. 20 Excess yield of dielectrons in the 10% most central Pb-Pb collisions at $\sqrt{s_{NN}} = 5.02\,\text{TeV}$ with respect to the expected $\mathrm{e}^+\mathrm{e}^-$ contributions from known hadronic sources, including (Cocktail2) or not including (Cocktail1) medium effects for the heavy-flavor contributions, and compared with predictions from the model of Rapp [57] (left) and from the PHSD transport approach [173] (right). Figure taken from [172].

4.5 Dileptons and the QCD phase diagram

One of the most challenging aims of contemporary heavy-ion-collision research is the identification of observables indicating changes in the nature of the confinement-deconfinement or the chiral phase transitions, e.g., the cross-over transition at low baryochemical potential to a first-order transition at higher net-baryon densities with a critical point at the end of the corresponding phase-transition line in the QCD phase diagram. This has been the motivation for a concise "beam-energy scan" at RHIC and in the future at FAIR.

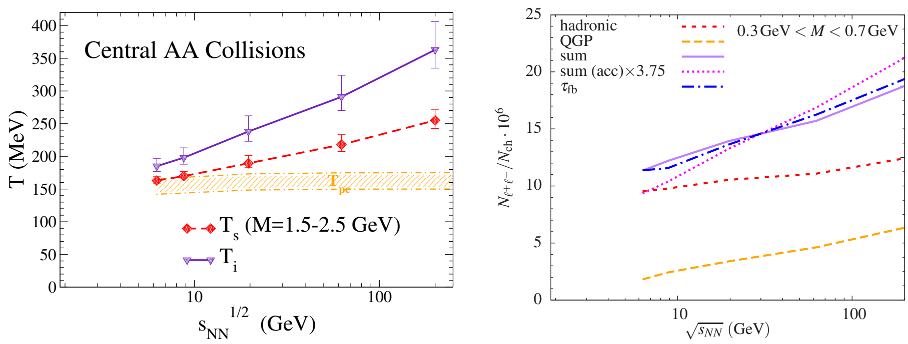

Fig. 21 Left panel: Excitation function of the inverse-slope parameter, $T_{\rm s}$, from intermediate-mass dilepton spectra ($M = 1.5$-2.5 GeV, diamonds connected with a dashed line) and initial temperature $T_{\rm i}$ (triangles connected with a solid line) in central heavy-ion collisions ($A \simeq 200$). The error bars on $T_{\rm s}$ and $T_{\rm i}$ correspond to a variation in the initial longitudinal fireball size, z_0, by ±30% around the central values. The hatched area schematically indicates the pseudo-critical temperature regime at vanishing (and small) baryochemical potential as extracted from various quantities computed in lQCD [174]. **Right panel:** Excitation function of low-mass thermal dilepton radiation ("excess spectra") in 0-10% central AA collisions ($A \simeq 200$), integrated over the mass range $M = 0.3$ GeV-0.7 GeV, for QGP (dashed line) and in-medium hadronic (short-dashed line) emission and their sum (solid line). The underlying fireball lifetime (dot-dashed line) is given by the right vertical scale. Figures taken from [147]

Since electromagnetic probes are emitted during all stages of the fireball evolution, leaving the hot and dense medium nearly unaffected by final-state interactions, they provide information not only about the in-medium properties of the em. current-current correlation function but also about the space-time evolution of the medium. Together with future high-precision measurements of dilepton production in heavy-ion collisions at various beam energies and for different system sizes, theoretical studies may also shed light on the phase structure of strongly interacting matter. E.g., the slope of the invariant-mass spectrum in the mass region $m_\phi < M_{\ell^+\ell^-} < m_{J/\psi}$ leads to a space-time weighted average of the invariant temperature of the medium (i.e., without blue shifts from radial flow as for slopes of $q_{\rm t}$ spectra, cf. the discussion in [85]), provided the hadronic cocktail, the contribution from decays of correlated D-$\overline{\rm D}$ (at higher beam energies also B-$\overline{\rm B}$) decay, and Drell-Yan pairs can be subtracted from the experimental data with sufficient precision.

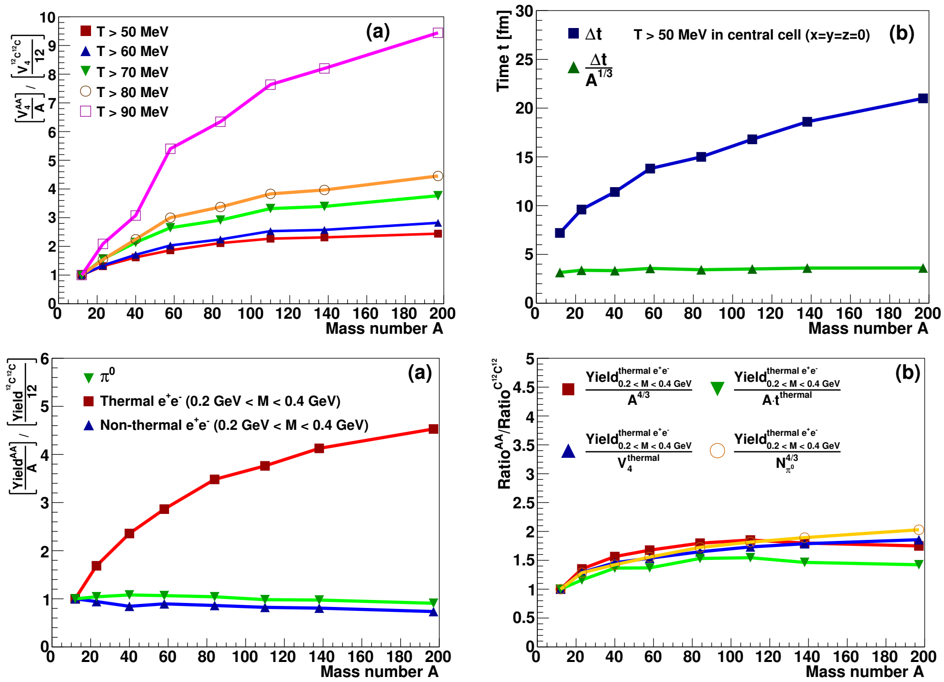

Fig. 22 Upper panels: (a) Ratio of the thermal four-volume V_4 for different temperatures to the mass number A of the colliding nuclei. (b) Time duration over which the central cell of the coarse-graining grid (for $x = y = z = 0$) emits thermal dileptons. **Lower panels:** (a) Ratio of the thermal (red squares) and non-thermal dilepton yield (blue triangles) in the invariant-mass range from 0.2 to 0.4 GeV/c^2 to the mass number A of the colliding nuclei, and the number of π^0 (green triangles). The results are normalized to the ratio obtained with $^{12}\mathrm{C} + {}^{12}\mathrm{C}$ collisions. (b) Ratio of the thermal dilepton yield in the invariant mass range from 0.2 to 0.4 GeV/c^2 scaled by various quantities. All four plots show the results for central collisions and a collision energy $E_{\mathrm{lab}} = 1.76$ AGeV. Figures taken from [111]

In [147] we have explored the possibilities for such studies within the above discussed theoretical model for dilepton production using the thermal-fireball parameterization of the medium, assuming the cross-over EoS (combining a hadron-resonance gas with a lQCD EoS as discussed in Sect. 3.3) for beam energies corresponding to center-mass energies in the range $\sqrt{s_{NN}} = 6.3$ GeV-200 GeV. We have determined the average temperature from the slopes of the invariant-mass spectrum of dileptons by fitting the dilepton spectrum in the range $M_{\ell^+\ell^-} = 1.5$-2.5 GeV to

$$\frac{\mathrm{d}R_{\ell^+\ell^-}}{\mathrm{d}M_{\ell^+\ell^-}} \propto (MT)^{3/2} \exp\left(-\frac{M_{\ell^+\ell^-}}{T}\right). \tag{79}$$

Since in this mass range $M_{\ell^+\ell^-} \ll T$ the average is weighted towards the hot and early phases of the fireball evolution. As can be seen in the left panel of Fig. 21 the resulting "slope temperatures" are smoothly increasing with beam energy and ranging from $T_{\mathrm{s}} \simeq 160$ MeV at $\sqrt{s_{NN}} = 6$ GeV to 260 MeV at $\sqrt{s_{NN}} = 200$ GeV. The values at the higher beam energies are clearly above the pseudo-critical temperature of $T_{\mathrm{c}} \simeq$

160 MeV but considerably lower than the initial fireball temperatures. This difference becomes smaller at the lower beam energies which is due to the (pseudo-)latent heat in the transition. This indicates that the beam-energy range around 10 GeV is promising to map out the phase-transition region, maybe indicating the onset of a first-order transition by developing a plateau of the slope curve, resembling a "caloric curve".

Further, for a given model for the dilepton-production rates, together with the determination of the fireball parameters from the hadronic observables (cf. Sect. 3.3) the total yield of dileptons is a quite precise measure for the fireball lifetime. This is shown in Fig. 21: The yield is determined by integrating the invariant-mass spectra over the range $M_{\ell^+\ell^-} = 0.3$-0.7 GeV, which is just below the ρ- and ω-vacuum mass, so that it consists of contributions from both partonic and hadronic sources and is quite representative for the dilepton enhancement due to medium effects, dominated by interactions of the vector mesons with baryons. As can be seen, the yield follows closely the proper lifetime τ_{fb} of the fireball. It is important to note that this correlation is disturbed by either changing the invariant-mass range or by using yields within the typical single-electron cuts describing the detector acceptance (e.g., $p_{\text{t}} > 0.2$ GeV, $y < 0.9$ for the STAR detector). Thus for such studies the availability of fully acceptance-corrected dilepton excess spectra is mandatory.

In [111] we have made similar studies concerning the system-size dependence of the bulk-medium dynamics at GSI-SIS energy, $E_{\text{lab}} = 1.76\ A\text{GeV}$, within the coarse-grained transport approach (cf. Sect. 4.1). At these low energies one expects that the lifetime of the medium is defined by the time the colliding nuclei overlap, forming a highly excited hadronic medium dominated by baryons. This can be confirmed by investigating the bulk properties and associated with dilepton observables within the coarse-grained transport approach. In the upper panels of Fig. 22 the "thermal four-volume" is plotted, i.e., the sum of all spacetime cells $\Delta V \Delta t$ for which the temperature, obtained from the coarse-graining procedure (as described in Sect. 3.3), is above various given values as indicated in plot (a). Since the total volume of each of the nuclei is $V_{\text{nucl}} \propto A$ and the lifetime of the thermal medium is expected to be determined by the time the nuclei overlap during the collision one concludes that $\Delta t \propto r_{\text{Nucl}} \propto A^{1/3}$, and this is indeed confirmed in plot (b) by the fact that $\Delta t / A^{1/3} \simeq \text{const.}$

Also in Fig. 3.3 the system-size dependence of the e^+e^- yields (in the mass window $M_{\text{e}^+\text{e}^-} = 0.2$ GeV-0.4 GeV) for emission from the medium ("thermal dileptons") and from ρ decays after thermal freeze-out ("non-thermal dileptons") as well as of neutral pions is shown. Since the "thermal dileptons" are emitted during the entire fireball evolution, one expects a scaling with the four-volume. On the other hand, the "non-thermal dilepton" as well as the pion yield is determined by the situation at thermal freezeout and thus scales with the three-volume of the corresponding cells ("freeze-out hypersurface") with coarse-graining temperatures below 50 MeV. This is approximately confirmed by plot (b): Scaling the yield with $A^{4/3}$, $A \cdot t^{\text{thermal}}$, V_4^{thermal}, or $N_{\pi_0}^{4/3}$ leads to a roughly flat system-size dependence.

As we have demonstrated in all these studies, dilepton and photon production in heavy-ion collisions can be well described with partonic and effective hadronic models for the in-medium em. current-current correlation function. Thus, together with adequate descriptions of the bulk-medium evolution, these techniques provide a promising tool to understand probable signals of the details of the QCD phase diagram as soon as high-precision data on dileptons and photons in heavy-ion collisions at various beam energies become available in the future. Particularly, when deviations from the here provided results are observed, sensitivity to Equations of State with different phase-transition properties may be reached.

Recently the STAR collaboration has extracted the space-time averaged temperatures from the measured acceptance corrected dielectron excess spectra within the beam-energy-scan program (BES II) [151]. Interestingly they fitted to both, low-mass (LMR) and intermediate-mass (IMR) regions. This is achieved by fitting the $\mathrm{e}^+\mathrm{e}^-$-invariant-mass spectra in the regions 0.4 GeV $< M_{\mathrm{e}^+\mathrm{e}^-} <$ 1.2 GeV for the LMR and 1.0 GeV $< M_{\mathrm{e}^+\mathrm{e}^-} <$ 2.9 GeV for the IMR. In the LMR the fit is to an ansatz function of the shape

$$\frac{\mathrm{d}N_{\mathrm{e}^+\mathrm{e}^-}}{\mathrm{d}N} \propto \Gamma_{\mathrm{e}^+\mathrm{e}^-} f_{\mathrm{BW}}(M) M^{3/2} \exp(-M/T) \tag{80}$$

with the relativistic Breit-Wigner distribution,

$$f_{\mathrm{BW}}(M) = \frac{M M_0}{(M_0^2 - M^2)^2 + M_0^2 \Gamma^2(M)}, \quad \Gamma(M) = \Gamma_0 \frac{M_0}{M} \left(\frac{M^2 - 4m_\pi^2}{M_0^2 - 4m_\pi^2} \right)^{3/2} \tag{81}$$

and the dilepton phase-space factor,

$$\Gamma_{\mathrm{e}^+\mathrm{e}^-} \propto \left(1 + \frac{2m_{\mathrm{e}}^2}{M^2}\right) \sqrt{1 - \frac{4m_{\mathrm{e}}^2}{M^2}}. \tag{82}$$

For the IMR the spectral function is assumed to be flat, i.e., fitting the excess yiels to a function $\propto M^{3/2} \exp(-M/T)$. In the IMR both the correlated-$\mathrm{D}\overline{\mathrm{D}} - decay$ and the Drell"=Yan background are subtracted using corresponding pp cross sections ("hadronic cocktail"). The temperature fits as well as the extracted temperatures in both mass regions are shown in Fig. 23. The results are in accordance with the expectation that the space-time weighted average is biased towards lower temperatures and larger fireball volumes in the LMR vs. higher temperatures and lower fireball volumes in the IMR.

From the theoretical side, e.g., the exploitation of functional-renormalization-group methods that allow a consistent description of both the EoS and the in-medium spectral functions of the light vector mesons, can be a promising way for such further studies [180, 181].

5 Conclusions and Outlook

As has been summarized in this review the dilepton production in heavy-ion collisions is theoretically quite well understood in terms of models using hard-thermal-loop or input from lattice-QCD calculations of $q\bar{q}$ annihilation in the partonic and effective hadronic models in the hadronic stages of the fireball evolution to describe the in-medium electromagnetic current-current-correlation function and the (thermal) dilepton-production rates from the strongly interacting medium created in heavy-ion collisions over all beam-energy ranges. There are strong indications that chiral

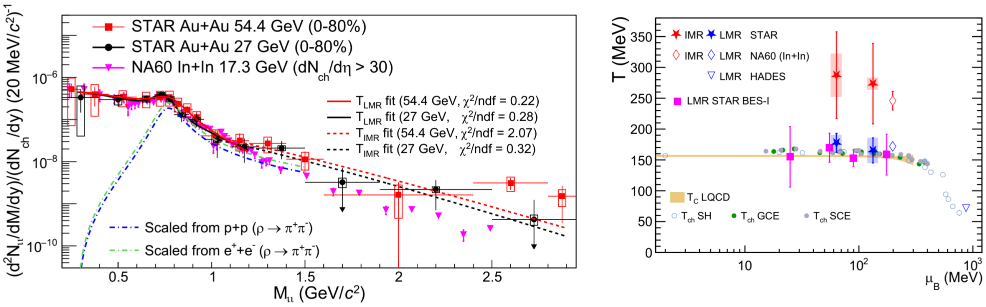

Fig. 23 Left: Thermal dielectron mass spectra from $\sqrt{s_{NN}} = 54.4\,\mathrm{GeV}$ (red squares) and 27 GeV (black dots) compared to the NA60 thermal dimuon data (magenta inverted triangles). ll denotes the dielectron or dimuon pairs. Dashed lines show the fitting curves for the corresponding temperature extractions. Dot-dashed lines display the expected vacuum-ρ spectra based on the p+p [89] and e$^+$e$^-$ [175] collision data. Vertical bars and boxes around data points represent the statistical and systematic uncertainties, respectively. Downward arrows indicate statistical uncertainties exceeding 100%. Right: Temperatures vs. baryon chemical potential. Temperatures extracted from in-medium ρ^0 ; the region of the later QGP stage (blue stars), and the region of the earlier QGP stage (red stars) from STAR data are compared to the temperatures extracted from NA60 data [144] (diamonds) and HADES data [176] (inverted triangle). Chemical freeze-out temperatures extracted from the statistical thermal models (SH, GCE, SCE) [177, 178] are shown as open and filled circles. The QCD critical temperature T_c at finite μ_{B} predicted by LQCD calculations [179] is shown as a yellow band. All temperatures are plotted at the μ_{B} determined at chemical freeze-out. Vertical bars and boxes around the data points represent the statistical and systematic uncertainties, respectively. Figure taken from [151].

symmetry is realized via the mirror-assignment/chiral doubler representation in the hadronic models, where the spontaneous breaking of chiral symmetry due to the formation of a quark condensate $\langle \overline{q}q \rangle \neq 0$ at lower temperatures is responsible only for the non-degeneracy of the mass spectra of chiral partners. It has also been demonstrated that accurate measurements of the invariant-mass spectrum of dileptons in the intermediate-mass region can be used to determine a space-time-evolution weighted average of the fireball temperature, provided non-thermal contributions like the dileptons from hard Drell-Yan processes and the decay of correlated open-heavy flavor (D and B) mesons can be reliably subtracted. The models also describe first measurements of polarization observables, and with realistic bulk-evolution models of the fireball it is possible to extract the life time of the strongly interacting medium [147].

This makes the electromagnetic probes a promising tool for constraining the rich phase diagram of strongly interacting (QCD) matter via high-precision measurements of the excitation function of dilepton emission: e.g., a first-order chiral phase transition should manifest itself in a plateau of the fireball temperatures ("latent heat") and if the "thermal trajectory" of the fireball comes close to a critical point this might be reflected in a prolonged fireball lifetime, indicating "critical slowing-down".

References

[1] Fukushima, K., Hatsuda, T.: The phase diagram of dense QCD. Rept. Prog. Phys. **74**, 014001 (2011)

[2] Karsch, F.: Lattice QCD at high temperature and density. Lect. Notes Phys. **583**, 209–249 (2002)

[3] Philipsen, O.: The QCD equation of state from the lattice. Prog. Part. Nucl. Phys. **70**, 55–107 (2013)

[4] Borsanyi, S., Endrodi, G., Fodor, Z., Hoelbling, C., Katz, S., *et al.*: Transition temperature and the equation of state from lattice QCD, Wuppertal-Budapest results. J. Phys. G **38**, 124101 (2011)

[5] Meisinger, P.N., Ogilvie, M.C.: Chiral symmetry restoration and Z(N) symmetry. Phys. Lett. B **379**, 163–168 (1996)

[6] Pisarski, R.D.: Quark gluon plasma as a condensate of SU(3) Wilson lines. Phys. Rev. D **62**, 111501 (2000)

[7] Fukushima, K.: Chiral effective model with the Polyakov loop. Phys. Lett. B **591**, 277–284 (2004)

[8] Megias, E., Ruiz Arriola, E., Salcedo, L.L.: Polyakov loop in chiral quark models at finite temperature. Phys. Rev. D **74**, 065005 (2006)

[9] Ratti, C., Thaler, M.A., Weise, W.: Phases of QCD: Lattice thermodynamics and a field theoretical model. Phys. Rev. D **73**, 014019 (2006)

[10] Ghosh, S.K., Mukherjee, T.K., Mustafa, M.G., Ray, R.: Susceptibilities and speed of sound from PNJL model. Phys. Rev. D **73**, 114007 (2006)

[11] Sasaki, C., Friman, B., Redlich, K.: Susceptibilities and the Phase Structure of a Chiral Model with Polyakov Loops. Phys. Rev. D **75**, 074013 (2007)

[12] Kashiwa, K., Kouno, H., Matsuzaki, M., Yahiro, M.: Critical endpoint in the Polyakov-loop extended NJL model. Phys. Lett. B **662**, 26–32 (2008)

[13] Kovacs, P., Szep, Z.: The critical surface of the $\mathrm{SU}(3)_\mathrm{L} \times \mathrm{SU}(3)_\mathrm{R}$ chiral quark model at non-zero baryon density. Phys. Rev. D **75**, 025015 (2007)

[14] Schäfer, B.-J., Pawlowski, J.M., Wambach, J.: The Phase Structure of the Polyakov–Quark-Meson Model. Phys. Rev. D **76**, 074023 (2007)

[15] Mao, H., Jin, J., Huang, M.: Phase diagram and thermodynamics of the Polyakov linear sigma model with three quark flavors. J. Phys. G **37**, 035001 (2010)

[16] Gupta, U.S., Tiwari, V.K.: Meson masses and mixing angles in the 2+1 flavor Polyakov quark meson sigma model and symmetry restoration effects. Phys. Rev. D **81**, 054019 (2010)

[17] Herbst, T.K., Pawlowski, J.M., Schaefer, B.-J.: The phase structure of the

Polyakov–quark-meson model beyond mean field. Phys. Lett. B **696**, 58–67 (2011)

[18] Marko, G., Szep, Z.: Influence of the Polyakov loop on the chiral phase transition in the two flavor chiral quark model. Phys. Rev. D **82**, 065021 (2010)

[19] Schaefer, B.-J.: Fluctuations and the QCD Phase Diagram. Phys. Atom. Nucl. **75**, 741–743 (2012)

[20] McLerran, L., Pisarski, R.D.: Phases of cold, dense quarks at large N_c. Nucl. Phys. A **796**, 83–100 (2007)

[21] Hidaka, Y., McLerran, L.D., Pisarski, R.D.: Baryons and the phase diagram for a large number of colors and flavors. Nucl. Phys. A **808**, 117–123 (2008)

[22] Jungnickel, D.U., Wetterich, C.: Effective action for the chiral quark-meson model. Phys. Rev. D **53**, 5142–5175 (1996)

[23] Schaefer, B.-J., Pirner, H.-J.: Renormalization group flow and equation of state of quarks and mesons. Nucl. Phys. A **660**, 439–474 (1999)

[24] Tetradis, N.: The Quark meson model and the phase diagram of two flavor QCD. Nucl. Phys. A **726**, 93–119 (2003)

[25] Schaefer, B.-J., Wambach, J.: The Phase diagram of the quark meson model. Nucl. Phys. A **757**, 479–492 (2005)

[26] Schaefer, B.-J., Wambach, J.: Susceptibilities near the QCD (tri)critical point. Phys. Rev. D **75**, 085015 (2007)

[27] Schaefer, B.-J., Wambach, J.: Renormalization group approach towards the QCD phase diagram. Phys. Part. Nucl. **39**, 1025–1032 (2008)

[28] Skokov, V., Friman, B., Nakano, E., Redlich, K., Schaefer, B.-J.: Vacuum fluctuations and the thermodynamics of chiral models. Phys. Rev. D **82**, 034029 (2010)

[29] Nakano, E., Schaefer, B.-J., Stokic, B., Friman, B., Redlich, K.: Fluctuations and isentropes near the chiral critical endpoint. Phys. Lett. B **682**, 401–407 (2010)

[30] Skokov, V., Stokic, B., Friman, B., Redlich, K.: Meson fluctuations and thermodynamics of the Polyakov loop extended quark-meson model. Phys. Rev. C **82**, 015206 (2010)

[31] Skokov, V., Friman, B., Redlich, K.: Quark number fluctuations in the Polyakov loop-extended quark-meson model at finite baryon density. Phys. Rev. C **83**, 054904 (2011)

[32] Rapp, R., Wambach, J.: Chiral symmetry restoration and dileptons in relativistic heavy-ion collisions. Adv. Nucl. Phys. **25**, 1 (2000)

[33] Rapp, R., Wambach, J., Hees, H.: The Chiral Restoration Transition of QCD and Low Mass Dileptons. Landolt-Börnstein **23**, 134 (2010)

[34] Feinberg, E.L.: Direct Production of Photons and Dileptons in Thermodynamical Models of Multiple Hadron Production. Nuovo Cim. A **34**, 391 (1976)

[35] McLerran, L.D., Toimela, T.: Photon and Dilepton Emission from the Quark-Gluon Plasma: Some General Considerations. Phys. Rev. D **31**, 545 (1985)

[36] Gale, C., Kapusta, J.I.: Vector dominance model at finite temperature. Nucl. Phys. B **357**, 65–89 (1991)

[37] Peskin, M.E., Schroeder, D.V.: An Introduction to Quantum Field Theory. Addison-Wesley Publ. Comp., Reading, Massachusetts (1995)

[38] Bratkovskaya, E.L., Teryaev, O.V., Toneev, V.D.: Anisotropy of dilepton emission from nuclear collisions. Phys. Lett. B **348**, 283–289 (1995)

[39] Baym, G., Hatsuda, T., Strickland, M.: Virtual photon polarization in ultrarelativistic heavy-ion collisions. Phys. Rev. C **95**(4), 044907 (2017)

[40] Speranza, E., Jaiswal, A., Friman, B.: Virtual photon polarization and dilepton anisotropy in relativistic nucleus–nucleus collisions. Phys. Lett. B **782**, 395–400 (2018)

[41] Seck, F., Friman, B., Galatyuk, T., Hees, H., Rapp, R., Speranza, E., Wambach, J.: Polarization of thermal dilepton radiation. Phys. Lett. B **861**, 139267 (2025)

[42] Faccioli, P., Lourenço, C.: Particle Polarization in High Energy Physics. Springer, Cham (2022). https://doi.org/10.1007/978-3-031-08876-6

[43] Gao, H., Wu, X.-Y., Gale, C., Jackson, G., Jeon, S.: The polarization of thermal dileptons emitted in high-energy heavy-ion collisions (2026) arXiv:2605.30180 [nucl-th]

[44] Olive, K.A., *et al.*: Review of Particle Physics. Chin. Phys. C **38**, 090001 (2014)

[45] Sakurai, J.J.: Theory of strong interactions. Ann. Phys. (NY) **11**, 1–48 (1960)

[46] Gounaris, G.J., Sakurai, J.J.: Finite-Width Corrections to the Vector-Meson-Dominance Prediction for $\rho \to e^+e^-$. Phys. Rev. Lett. **21**(4), 244–247 (1968)

[47] Kroll, N.M., Lee, T.D., Zumino, B.: Neutral Vector Mesons and the Hadronic Electromagnetic Current. Phys. Rev. **157**, 1376 (1967)

[48] Yao, W.-M., *et al.*: Review of particle physics. J. Phys. G **33**, 1–1232 (2006)

[49] Nachtmann, O.: Elementary Particle Physics - Concepts and Phenomenology. Springer, Berlin, Heidelberg, New York, London, Paris, Tokyo (1990)

[50] Barate, R., *et al.*: Measurement of the spectral functions of axial-vector hadronic τ decays and determination of $\alpha_s(M_\tau^2)$. Eur. Phys. J. C **4**, 409–431 (1998)

[51] Rapp, R.: Dileptons in high-energy heavy-ion collisions. Pramana **60**, 675–686 (2003)

[52] Bando, M., Kugo, T., Uehara, S., Yamawaki, K., Yanagida, T.: Is the ρ Meson a Dynamical Gauge Boson of Hidden Local Symmetry? Phys. Rev. Lett. **54**, 1215 (1985)

[53] Bando, M., Kugo, T., Yamawaki, K.: Nonlinear Realization and Hidden Local Symmetries. Phys. Rept. **164**, 217–314 (1988)

[54] Harada, M., Yamawaki, K.: Hidden local symmetry at loop: A new perspective of composite gauge boson and chiral phase transition. Phys. Rept. **381**, 1–233 (2003)

[55] Harada, M., Sasaki, C.: Dropping ρ and A_1 meson masses at chiral phase transition in the generalized hidden local symmetry. Phys. Rev. D **73**, 036001 (2006)

[56] Harada, M., Sasaki, C., Weise, W.: Vector-axialvector mixing from a chiral effective field theory at finite temperature. Phys. Rev. D **78**, 114003 (2008)

[57] Rapp, R.: Dilepton Spectroscopy of QCD Matter at Collider Energies. Adv. High Energy Phys. **2013**, 148253 (2013)

[58] Cleymans, J., Fingberg, J., Redlich, K.: Transverse Momentum Distribution of Dileptons in Different Scenarios for the QCD Phase Transition. Phys. Rev. D **35**, 2153 (1987)

[59] Braaten, E., Pisarski, R.D., Yuan, T.-C.: Production of soft dileptons in the quark-gluon plasma. Phys. Rev. Lett. **64**, 2242 (1990)

[60] Ding, H.-T., Francis, A., Kaczmarek, O., Karsch, F., Laermann, E., *et al.*: Thermal dilepton rate and electrical conductivity: An analysis of vector current correlation functions in quenched lattice QCD. Phys. Rev. D **83**, 034504 (2011)

[61] Brandt, B.B., Francis, A., Meyer, H.B., Wittig, H.: Thermal Correlators in the ρ channel of two-flavor QCD. JHEP **1303**, 100 (2013)

[62] Kaczmarek, O., Laermann, E., Müller, M., Karsch, F., Ding, H.T., Mukherjee, S., Francis, A., Soeldner, W.: Thermal dilepton rates from quenched lattice QCD.

PoS **Confinement X**, 185 (2012)

[63] Rapp, R., Wambach, J.: Chiral symmetry restoration and dileptons in relativistic heavy ion collisions. Adv. Nucl. Phys. **25**, 1 (2000)

[64] Rapp, R., Chanfray, G., Wambach, J.: Medium modifications of the rho meson at CERN SPS energies. Phys. Rev. Lett. **76**, 368–371 (1996)

[65] Rapp, R., Chanfray, G., Wambach, J.: Rho meson propagation and dilepton enhancement in hot hadronic matter. Nucl. Phys. A **617**, 472–495 (1997)

[66] Urban, M., Buballa, M., Rapp, R., Wambach, J.: Momentum dependence of the pion cloud for ρ mesons in nuclear matter. Nucl. Phys. A **641**, 433 (1998)

[67] Rapp, R., Urban, M., Buballa, M., Wambach, J.: A microscopic calculation of photoabsorption cross sections on protons and nuclei. Phys. Lett. B **417**, 1 (1998)

[68] Rapp, R., Gale, C.: ρ properties in a hot meson gas. Phys. Rev. C **60**, 024903 (1999)

[69] Rapp, R., Wambach, J.: Low mass dileptons at the CERN SPS: Evidence for chiral restoration? Eur. Phys. J. A **6**, 415–420 (1999)

[70] Ericson, T., Weise, W.: Pions and Nuclei. Clarendon Press, Oxford, ??? (1988)

[71] Rapp, R., Wambach, J.: Pion properties in a hot pi N Delta gas. Nucl. Phys. A **573**, 626–640 (1994)

[72] Effenberger, M., Hombach, A., Teis, S., Mosel, U.: Photoabsorption on nuclei. Nucl. Phys. A **613**, 353–370 (1997)

[73] Peters, W., Post, M., Lenske, H., Leupold, S., Mosel, U.: The Spectral function of the rho meson in nuclear matter. Nucl. Phys. A **632**, 109–127 (1998)

[74] Machleidt, R., Holinde, K., Elster, C.: The Bonn Meson Exchange Model for the Nucleon Nucleon Interaction. Phys. Rept. **149**, 1–89 (1987)

[75] Friman, B., Pirner, H.J.: P-wave polarization of the rho meson and the dilepton spectrum in dense matter. Nucl. Phys. A **617**, 496–509 (1997)

[76] Armstrong, T.A., *et al.*: Total hadronic cross-section of gamma rays in hydrogen in the energy range 0.265 GeV to 4.215 GeV. Phys. Rev. D **5**, 1640–1652 (1972)

[77] Lepretre, A., Beil, H., Bergere, R., Carlos, P., Fagot, J., Veyssiere, A., Ahrens, J., Axel, P., Kneissl, U.: Total Photonuclear Absorption Cross-Section of Pb Measured with Quasimonochromatic Photons Between 25 MeV and 106 MeV. Phys. Lett. B **79**, 43–46 (1978)

[78] Ahrens, J., *et al.*: Measurement of the Total Cross-section for ^{235}U and ^{238}U Photofission in the Δ Resonance Region. Phys. Lett. B **146**, 303–306 (1984)

[79] Ahrens, J.: The Total Absorption of Photons by Nuclei. Nucl. Phys. A **446**, 229–239 (1985)

[80] Frommhold, T., Steiper, F., Henkel, W., Kneissl, U., Ahrens, J., Beck, R., Peise, J., Schmitz, M.: Total photofission cross-section for ^{238}U as a substitute for the photon absorption cross-section in the energy range of the first baryon resonances. Phys. Lett. B **295**, 28–31 (1992)

[81] Bianchi, N., *et al.*: Measurement of the total cross-section for ^{238}U photofission in the nucleon resonance region. Phys. Lett. B **299**, 219–222 (1993)

[82] Bianchi, N., *et al.*: Total hadronic photoabsorption cross-section on nuclei in the nucleon resonance region. Phys. Rev. C **54**, 1688–1699 (1996)

[83] Dey, M., Eletsky, V.L., Ioffe, B.L.: Mixing of vector and axial mesons at finite temperature: an Indication towards chiral symmetry restoration. Phys. Lett. B **252**, 620–624 (1990)

[84] Hees, H.v., Rapp, R.: Comprehensive interpretation of thermal dileptons at the SPS. Phys. Rev. Lett. **97**, 102301 (2006)

[85] Hees, H.v., Rapp, R.: Dilepton Radiation at the CERN Super Proton Synchrotron. Nucl. Phys. A **806**, 339 (2008)

[86] Steele, J.V., Yamagishi, H., Zahed, I.: Dilepton and Photon Emission Rates from a Hadronic Gas. Phys. Lett. B **384**, 255–262 (1996)

[87] Steele, J.V., Yamagishi, H., Zahed, I.: Dilepton and photon emission rates from a hadronic gas. II. Phys. Rev. D **56**, 5605–5617 (1997)

[88] Turbide, S., Rapp, R., Gale, C.: Hadronic production of thermal photons. Phys. Rev. C **69**, 014903 (2004)

[89] Aguilar-Benitez, M., *et al.*: Inclusive particle production in 400 GeV/c p p interactions. Z. Phys. C **50**, 405–426 (1991)

[90] Glück, M., Reya, E., Vogt, A.: Dynamical parton distributions of the proton and small x physics. Z. Phys. C **67**, 433–448 (1995)

[91] Spieles, C., Gerland, L., Hammon, N., Bleicher, M., Bass, S.A., Stöcker, H., Greiner, W., Lourenco, C., Vogt, R.: A Microscopic calculation of secondary Drell-Yan production in heavy ion collisions. Eur. Phys. J. C **5**, 349–355 (1998)

[92] Abreu, M.C., *et al.*: Dimuon enhancement in nucleus nucleus ultrarelativistic interactions. Nucl. Phys. A **661**, 538–541 (1999)

[93] Abreu, M.C., *et al.*: Dimuon and charm production in nucleus nucleus collisions at the CERN-SPS. Eur. Phys. J. C **14**, 443–455 (2000)

[94] Song, C.: Photon emission from hot hadronic matter described by an effective chiral Lagrangian. Phys. Rev. C **47**, 2861–2874 (1993)

[95] Gao, S., Gale, C.: Off-shell effects in dilepton production from hot interacting mesons. Phys. Rev. C **57**, 254–260 (1998)

[96] Hohler, P.M., Rapp, R.: Is ρ-Meson Melting Compatible with Chiral Restoration? Phys. Lett. B **731**, 103–109 (2014)

[97] Bearden, I.G., *et al.*: Collective expansion in high-energy heavy ion collisions. Phys. Rev. Lett. **78**, 2080–2083 (1997)

[98] Appelshäuser, H., *et al.*: Hadronic expansion dynamics in central Pb + Pb collisions at 158 GeV per nucleon. Eur. Phys. J. C **2**, 661–670 (1998)

[99] Antinori, F., *et al.*: Centrality dependence of the expansion dynamics in Pb Pb collisions at 158A GeV/c. J. Phys. G **27**, 2325–2344 (2001)

[100] Antinori, F., *et al.*: Expansion dynamics of Pb-Pb collisions at 40AGeV/c viewed by negatively charged hadrons. J. Phys. G **33**, 403–430 (2007)

[101] Adamova, D., *et al.*: Beam energy and centrality dependence of two pion Bose-Einstein correlations at SPS energies. Nucl. Phys. A **714**, 124–144 (2003)

[102] He, M., Fries, R.J., Rapp, R.: Ideal Hydrodynamics for Bulk and Multistrange Hadrons in $\sqrt{s_{NN}}$=200 AGeV Au-Au Collisions. Phys. Rev. C **85**, 044911 (2012)

[103] Hees, H., Gale, C., Rapp, R.: Thermal Photons and Collective Flow at the Relativistic Heavy-Ion Collider. Phys. Rev. C **84**, 054906 (2011)

[104] Hees, H., He, M., Rapp, R.: Pseudo-Critical Enhancement of Thermal Photons in Relativistic Heavy-Ion Collisions. Nucl. Phys. A **933**, 256 (2015)

[105] Abelev, B.I., *et al.*: Partonic flow and phi-meson production in Au + Au collisions at $\sqrt{s_{NN}} = 200$ GeV. Phys. Rev. Lett. **99**, 112301 (2007)

[106] Adler, S.S., *et al.*: Elliptic flow of identified hadrons in Au + Au collisions at $\sqrt{s_{NN}} = 200$ GeV. Phys. Rev. Lett. **91**, 182301 (2003)

[107] Adler, S.S., *et al.*: Identified charged particle spectra and yields in Au + Au collisions at $\sqrt{s_{NN}} = 200$ GeV. Phys. Rev. C **69**, 034909 (2004)

[108] Adams, J., *et al.*: Identified particle distributions in pp and Au+Au collisions at $\sqrt{s_{NN}} = 200$ GeV. Phys. Rev. Lett. **92**, 112301 (2004)

[109] Endres, S., Hees, H., Weil, J., Bleicher, M.: Coarse-graining approach for dilepton production at energies available at the CERN Super Proton Synchrotron. Phys. Rev. C **91**(5), 054911 (2015)

[110] Endres, S., Hees, H., Bleicher, M.: Photon and dilepton production at the Facility for Proton and Anti-Proton Research and beam-energy scan at the Relativistic Heavy-Ion Collider using coarse-grained microscopic transport simulations. Phys. Rev. C **93**(5), 054901 (2016)

[111] Endres, S., Hees, H., Weil, J., Bleicher, M.: Dilepton production and reaction dynamics in heavy-ion collisions at SIS energies from coarse-grained transport simulations. Phys. Rev. C **92**(1), 014911 (2015)

[112] Endres, S., Hees, H., Bleicher, M.: Energy, centrality and momentum dependence of dielectron production at collider energies in a coarse-grained transport approach. Phys. Rev. C **94**(2), 024912 (2016)

[113] Bass, S.A., Belkacem, M., Bleicher, M., Brandstetter, M., Bravina, L., *et al.*: Microscopic models for ultrarelativistic heavy ion collisions. Prog. Part. Nucl. Phys. **41**, 255–369 (1998)

[114] Bleicher, M., Zabrodin, E., Spieles, C., Bass, S.A., Ernst, C., *et al.*: Relativistic hadron hadron collisions in the ultrarelativistic quantum molecular dynamics model. J. Phys. G **25**, 1859–1896 (1999)

[115] Petersen, H., Bleicher, M., Bass, S.A., Stöcker, H.: UrQMD v2.3: Changes and Comparisons (2008) arXiv: 0805.0567 [hep-ph]

[116] Florkowski, W., Ryblewski, R.: Highly-anisotropic and strongly-dissipative hydrodynamics for early stages of relativistic heavy-ion collisions. Phys. Rev. C **83**, 034907 (2011)

[117] Florkowski, W., Martinez, M., Ryblewski, R., Strickland, M.: Anisotropic hydrodynamics. Nucl. Phys. A **904-905**, 803–806 (2013)

[118] Molnár, E., Niemi, H., Rischke, D.H.: Closing the equations of motion of anisotropic fluid dynamics by a judicious choice of a moment of the Boltzmann equation. Phys. Rev. D **94**(12), 125003 (2016)

[119] Zschiesche, D., Schramm, S., Schaffner-Bielich, J., Stöcker, H., Greiner, W.: Particle ratios at RHIC: Effective hadron masses and chemical freezeout. Phys. Lett. B **547**, 7–14 (2002)

[120] Petersen, H., Steinheimer, J., Burau, G., Bleicher, M., Stöcker, H.: A Fully Integrated Transport Approach to Heavy Ion Reactions with an Intermediate Hydrodynamic Stage. Phys. Rev. C **78**, 044901 (2008)

[121] Papazoglou, P., Zschiesche, D., Schramm, S., Schaffner-Bielich, J., Stöcker, H., Greiner, W.: Nuclei in a chiral SU(3) model. Phys. Rev. C **59**, 411–427 (1999)

[122] Zschiesche, D., Zeeb, G., Schramm, S.: Phase structure in a hadronic chiral model. J. Phys. G **34**, 1665–1672 (2007)

[123] Linnyk, O., Cassing, W., Manninen, J., Bratkovskaya, E.L., Ko, C.M.: Analysis of dilepton production in Au+Au collisions at $\sqrt{s_{NN}} = 200\,\mathrm{GeV}$ within the Parton-Hadron-String Dynamics (PHSD) transport approach. Phys. Rev. C **85**, 024910 (2012)

[124] Linnyk, O., Bratkovskaya, E.L., Ozvenchuk, V., Cassing, W., Ko, C.M.: Dilepton production in nucleus-nucleus collisions at top SPS energy within the Parton-Hadron-String Dynamics (PHSD) transport approach. Phys. Rev. C **84**, 054917 (2011) https://doi.org/10.1103/PhysRevC.84.054917

[125] Linnyk, O., Cassing, W., Manninen, J., Bratkovskaya, E.L., Gossiaux, P.B., Aichelin, J., Song, T., Ko, C.M.: Dilepton production in proton-proton and Pb+Pb collisions at $\sqrt{s_{NN}} = 2.76$ TeV. Phys. Rev. C **87**(1), 014905 (2013)

[126] Cassing, W., Bratkovskaya, E.L.: Parton transport and hadronization from the dynamical quasiparticle point of view. Phys. Rev. C **78**, 034919 (2008)

[127] Ehehalt, W., Cassing, W.: Relativistic transport approach for nucleus nucleus collisions from SIS to SPS energies. Nucl. Phys. A **602**, 449–486 (1996)

[128] Bratkovskaya, E.L., Cassing, W.: Dilepton production from AGS to SPS energies within a relativistic transport approach. Nucl. Phys. A **619**, 413–446 (1997)

[129] Cassing, W., Bratkovskaya, E.L.: Hadronic and electromagnetic probes of hot and dense nuclear matter. Phys. Rept. **308**, 65–233 (1999)

[130] Bratkovskaya, E.L., Cassing, W.: Dilepton production and off-shell transport dynamics at SIS energies. Nucl. Phys. A **807**, 214–250 (2008)

[131] Porter, R.J., *et al.*: Dielectron cross-section measurements in nucleus-nucleus reactions at 1 AGeV. Phys. Rev. Lett. **79**, 1229–1232 (1997)

[132] Agakishiev, G., *et al.*: Hyperon production in Ar+KCl collisions at 1.76A GeV. Eur. Phys. J. A **47**, 21 (2011)

[133] Galatyuk, T. private communication (2014)

[134] Galatyuk, T.: HADES overview. Nucl. Phys. A **931**, 41–51 (2014)

[135] https://www-hades.gsi.de/

[136] https://macdls.lbl.gov/DLS_WWW_Files/Filter_4.1/

[137] Arnaldi, R., *et al.*: First results on angular distributions of thermal dileptons in nuclear collisions. Phys. Rev. Lett. **102**, 222301 (2009)

[138] Agakishiev, G., *et al.*: Dielectron production in Ar+KCl collisions at 1.76A GeV. Phys. Rev. C **84**, 014902 (2011)

[139] Agakishiev, G., *et al.*: Dielectron production in Ar+KCl collisions at 1.76AGeV. Phys. Rev. C **84**, 014902 (2011)

[140] Góes-Hirayama, R., Elfner, H.: Distinguishing the sources of dielectron anisotropic flow at low beam energies. Phys. Rev. C **110**(6), 064903 (2024)

[141] Weil, J., *et al.*: Particle production and equilibrium properties within a new hadron transport approach for heavy-ion collisions. Phys. Rev. C **94**(5), 054905 (2016)

[142] Galatyuk, T.: Recent Results from HADES. JPS Conf. Proc. **32**, 010079 (2020)

[143] Schild, N.: Characterising the hot and dense fireball with virtual photons at HADES. PoS **HardProbes2023**, 072 (2024)

[144] Arnaldi, R., *et al.*: Evidence for the production of thermal-like muon pairs with masses above 1 GeV/c^2 in 158 A GeV Indium-Indium Collisions. Eur. Phys. J. C **59**, 607–623 (2009)

[145] Specht, H.J.: Thermal Dileptons from Hot and Dense Strongly Interacting Matter. AIP Conf.Proc. **1322**, 1–10 (2010)

[146] Arnaldi, R., *et al.*: NA60 results on thermal dimuons. Eur. Phys. J. C **61**, 711–720 (2009)

[147] Rapp, R., Hees, H.: Thermal Dileptons as Fireball Thermometer and Chronometer. Phys. Lett. B **753**, 586–590 (2016)

[148] Arnaldi, R., *et al.*: First measurement of the ρ spectral function in high-energy nuclear collisions. Phys. Rev. Lett. **96**, 162302 (2006)

[149] Arnaldi, R., *et al.*: Evidence for radial flow of thermal dileptons in high-energy nuclear collisions. Phys. Rev. Lett. **100**, 022302 (2008)

[150] Damjanovic, S., *et al.*: NA60 results on the rho spectral function in In In collisions. Nucl. Phys. A **783**, 327–334 (2007)

[151] Aboona, B.E., *et al.*: Temperature measurement of Quark-Gluon plasma at different stages. Nature Commun. **16**(1), 9098 (2025)

[152] Rapp, R.: Signatures of thermal dilepton radiation at RHIC. Phys. Rev. C **63** (2001)

[153] Cassing, W., Bratkovskaya, E.L., Rapp, R., Wambach, J.: Probing the rho spectral function in hot and dense nuclear matter by dileptons. Phys. Rev. C **57**, 916–921 (1998)

[154] Adamczyk, L., *et al.*: Measurements of Dielectron Production in Au+Au Collisions at $\sqrt{s_{\rm NN}}$ = 200GeV from the STAR Experiment. Phys. Rev. C **92**(2), 024912 (2015)

[155] Laine, M.: NLO thermal dilepton rate at non-zero momentum. JHEP **11**, 120 (2013)

[156] Jackson, G.: Two-loop thermal spectral functions with general kinematics. Phys. Rev. D **100**(11), 116019 (2019)

[157] Wu, X.-Y., Du, L., Gale, C., Jeon, S.: Probing the equilibration of the QCD matter created in heavy-ion collisions with dileptons. Phys. Rev. C **110**(5), 054904 (2024)

[158] Wu, X.-Y., Gao, H., Forster, B., Gale, C., Jackson, G., Jeon, S.: Thermal Dilepton Polarization and Dynamics of the QCD Plasma in Relativistic Heavy-Ion Collisions. Phys. Rev. Lett. **134**(24), 242301 (2025)

[159] Schenke, B., Tribedy, P., Venugopalan, R.: Fluctuating Glasma initial conditions and flow in heavy ion collisions. Phys. Rev. Lett. **108**, 252301 (2012)

[160] Schenke, B., Tribedy, P., Venugopalan, R.: Event-by-event gluon multiplicity, energy density, and eccentricities in ultrarelativistic heavy-ion collisions. Phys. Rev. C **86**, 034908 (2012)

[161] Kurkela, A., Mazeliauskas, A., Paquet, J.-F., Schlichting, S., Teaney, D.: Effective kinetic description of event-by-event pre-equilibrium dynamics in high-energy heavy-ion collisions. Phys. Rev. C **99**(3), 034910 (2019)

[162] Kurkela, A., Mazeliauskas, A., Paquet, J.-F., Schlichting, S., Teaney, D.: Matching the Nonequilibrium Initial Stage of Heavy Ion Collisions to Hydrodynamics with QCD Kinetic Theory. Phys. Rev. Lett. **122**(12), 122302 (2019)

[163] Gale, C., Paquet, J.-F., Schenke, B., Shen, C.: Multimessenger heavy-ion collision physics. Phys. Rev. C **105**(1), 014909 (2022) https://doi.org/10.1103/PhysRevC.105.014909 arXiv:2106.11216 [nucl-th]

[164] Paquet, J.-F., Shen, C., Denicol, G.S., Luzum, M., Schenke, B., Jeon, S., Gale, C.: Production of photons in relativistic heavy-ion collisions. Phys. Rev. C **93**(4), 044906 (2016)

[165] Schenke, B., Jeon, S., Gale, C.: (3+1)D hydrodynamic simulation of relativistic heavy-ion collisions. Phys. Rev. C **82**, 014903 (2010)

[166] Schenke, B., Jeon, S., Gale, C.: Elliptic and triangular flow in event-by-event (3+1)D viscous hydrodynamics. Phys. Rev. Lett. **106**, 042301 (2011)

[167] Cooper, F., Frye, G.: Single-particle distribution in the hydrodynamic and statistical thermodynamic models of multiparticle production. Phys. Rev. D **10**, 186 (1974)

[168] Ryu, S., Paquet, J.-F., Shen, C., Denicol, G.S., Schenke, B., Jeon, S., Gale, C.: Importance of the Bulk Viscosity of QCD in Ultrarelativistic Heavy-Ion Collisions. Phys. Rev. Lett. **115**(13), 132301 (2015)

[169] Schenke, B., Shen, C., Tribedy, P.: Running the gamut of high energy nuclear collisions. Phys. Rev. C **102**(4), 044905 (2020)

[170] Shen, C., Qiu, Z., Song, H., Bernhard, J., Bass, S., Heinz, U.: The iEBE-VISHNU code package for relativistic heavy-ion collisions. Comput. Phys. Commun. **199**, 61–85 (2016)

[171] Camarda, S., *et al.*: DYTurbo: Fast predictions for Drell-Yan processes. Eur. Phys. J. C **80**(3), 251 (2020). [Erratum: Eur. Phys. J. C 80, 440 (2020)]

[172] Acharya, S., *et al.*: Dielectron production in central Pb-Pb collisions at $\sqrt{s_{NN}} = 5.02\,\mathrm{TeV}$. Phys. Rev. C **112**(5), 054906 (2025)

[173] Song, T., Cassing, W., Moreau, P., Bratkovskaya, E.: Open charm and dileptons from relativistic heavy-ion collisions. Phys. Rev. C **97**(6), 064907 (2018)

[174] Borsanyi, S., Fodor, Z., Hoelbling, C., Katz, S.D., Krieg, S., Ratti, C., Szabo, K.K.: Is there still any T_c mystery in lattice QCD? Results with physical masses in the continuum limit III. JHEP **09**, 073 (2010)

[175] Derrick, M., *et al.*: Neutral $\mathrm{K}^*(890)$ and ρ^0 Meson Production in $\mathrm{e}^+\mathrm{e}^-$ Annihilation at $\sqrt{s} = 29\,\mathrm{GeV}$. Phys. Lett. B **158**, 519–524 (1985)

[176] Adamczewski-Musch, J., *et al.*: Probing dense baryon-rich matter with virtual photons. Nature Phys. **15**(10), 1040–1045 (2019)

[177] Andronic, A., Braun-Munzinger, P., Redlich, K., Stachel, J.: Decoding the phase structure of QCD via particle production at high energy. Nature **561**(7723), 321–330 (2018)

[178] Adamczyk, L., *et al.*: Bulk Properties of the Medium Produced in Relativistic Heavy-Ion Collisions from the Beam Energy Scan Program. Phys. Rev. C **96**(4), 044904 (2017)

[179] Bazavov, A., *et al.*: Chiral crossover in QCD at zero and non-zero chemical potentials. Phys. Lett. B **795**, 15–21 (2019)

[180] Tripolt, R.-A., Smekal, L., Wambach, J.: Spectral functions and in-medium properties of hadrons. Int. J. Mod. Phys. E **26**(01n02), 1740028 (2017)

[181] Jung, C., Rennecke, F., Tripolt, R.-A., Smekal, L., Wambach, J.: In-Medium Spectral Functions of Vector- and Axial-Vector Mesons from the Functional Renormalization Group. Phys. Rev. D **95**(3), 036020 (2017)